



---

## Spectral Method Applied to Thermochemical Non-Equilibrium Reentry Flows in 2D: Five Species – High Order Analysis

Edisson Sávio de Góes Maciel

Instituto Tecnológico de Aeronáutica (ITA) – Rua Santa Clara, 245 – Cx. Postal: 2029, 12.243-970 – São José dos Campos – SP – Brazil

---

**Abstract** In the present work, a study involving a spectral method to solve the reactive Euler and Navier-Stokes equations is performed. The Euler and Navier-Stokes equations, in conservative and finite volume contexts, employing structured spatial discretization, on a condition of thermochemical non-equilibrium, are studied. The spectral method presented in this work employs collocation points and variants of Chebyshev and Legendre interpolation functions are analyzed. High-order studies are accomplished to verify the accuracy of the spectral method. The “hot gas” hypersonic flows around a blunt body, around a double ellipse, and around a reentry capsule in two-dimensions are simulated. The Van Leer and the Liou and Steffen Jr. flux vector splitting algorithms are applied to execute the numerical experiments. The Euler backward integration method is employed to march the schemes in time. The convergence process is accelerated to steady state condition through a spatially variable time step procedure, which has proved effective gains in terms of computational acceleration (see Maciel). The reactive simulations involve Earth atmosphere chemical model of five species and seventeen reactions, based on the Saxena and Nair model. N, O, N<sub>2</sub>, O<sub>2</sub>, and NO species are used to accomplish the numerical comparisons. The results have indicated that the Chebyshev collocation point variants are more accurate in terms of stagnation pressure estimations. Errors inferior to 16.16% were found for this parameter in the inviscid case, while inferior to 11.55% for the viscous case. The Legendre collocation point variants are more accurate in terms of the lift coefficient estimations. Moreover, the Legendre collocation point variants are more computationally efficient and cheaper.

**Keywords** Hypersonic flow; thermochemical non-equilibrium reentry flows; reactive Euler and Navier-Stokes equations; high order accuracy; Van Leer scheme; Liou and Steffen Jr. scheme; spectral method

---

### 1. Introduction

There are several approaches for computationally modeling fluid dynamics. These include finite difference, finite element, and spectral methods to name a few. Finite element and finite difference methods are frequently used and offer a wide range of well-known numerical schemes. These schemes can vary in terms of computational accuracy, but are typically of lower order of accuracy. If a more accurate solution is desired, it is common practice to refine the mesh either globally or in a region of interest. This can often be a complicated or time consuming process as global mesh refinement will greatly increase the computation time while local refinement requires an elaborated refinement operation [1].

Alternatively, polynomial refinement has been used to improve the solution accuracy and has been shown to converge more quickly than mesh refinement in some cases [2-3]. For finite difference methods, polynomial refinement is performed by including neighboring node values in a higher order polynomial [4]. This can increase the complexity of the scheme especially near the boundaries where nodes do not exist to construct the



higher order polynomials. Finite element methods instead increase the number of unknown values within the cell itself to construct a higher order solution [5].

A scheme with a very high formal order of accuracy will not necessarily always produce the highest resolution. [6] demonstrated that a spectral-like scheme with a formal fourth-order accuracy produced a much more highly resolved solution than schemes with higher formal orders of accuracy when comparing modified wave numbers. Therefore, formal order of accuracy does not provide a comprehensive basis for selecting the best solution procedure. State-of-art methods such as spectral methods fall into this category.

Spectral methods are considered a class of solution techniques using sets of known functions to solve differential equations [7]. Such methods are generally considered high order and capable of obtaining solutions with a high resolution. Unlike finite-difference and finite-element methods, spectral methods utilize an expansion in terms of global, rather than local, basis functions to represent the solution of a differential equation. When properly applied, these techniques accurately resolve phenomena on the scale of the mesh spacing. The order of truncation error decay with mesh refinement is also higher than which can be achieved with finite-difference and finite-element methods. For problems with smooth solutions, it is possible to produce spectral method whose truncation error goes to zero as faster than any finite power of the mesh spacing (exponential convergence).

Spectral methods may be viewed as an extreme development of the class of discretization schemes known by the generic name of method of weighted residuals (MWR) [8]. The key elements of the MWR are the trial functions (also called the expansion or approximating functions) and the test functions (also known as weighted functions). The trial functions are used as the basis functions for a truncated series expansion of the solution that, when substituted into the differential equation, produces the residual. The test functions are used to enforce the minimization of the residual.

The choice of the trial functions is what distinguishes the spectral methods from the element and finite difference methods. The trial functions for spectral methods are infinitely differentiable global functions (Typically, they are tensor products of the eigenfunctions of singular Sturm-Liouville problems). In the case of finite element methods, the domain is divided into small elements and a trial function is specified in each element. The trial functions are thus local in character and well suited for handling complex geometries. The finite difference trial functions are likewise local.

The choice of test function distinguishes between Galerkin and collocation approaches. In the Galerkin approach, the test functions are the same as the trial functions, whereas in the collocation approach the test functions are translated Dirac delta functions. In other words, the Galerkin approach is equivalent to a least-square approximation, whereas the collocation approach requires the differential equations to be solved exactly at the collocation points.

The collocation approach is the simplest of the MWR and appears to have been first used by [9] in his study of electronic energy bands in metals. A few years later, [10] applied this method to the problem of torsion in square prism. [11] developed it as a general method for solving ordinary differential equations. They used a variety of trials functions and an arbitrary distribution of collocation points. The work of [12] established for the first time that a proper choice of the trial functions and the distribution of collocation points are crucial to the accuracy of the solution. Perhaps he should be credited with laying down the foundation of the orthogonal collocation method.

Spectral methods have been used on one-dimensional, compressible flow problems with piecewise linear solutions by [13-14]. These reports demonstrated that spectral methods, when combined with appropriate filtering techniques, can capture one-dimensional shock waves in otherwise featureless flows. A different sort of demonstration was provided by [15]. They exhibited spectral solutions of compressible flows with nontrivial structures in the smooth regions.

Renewed interest in the area of hypersonic flight has brought Computational Fluid Dynamics (CFD) to the forefront of fluid flow research [16]. Many years have seen a quantum leap in advancements made in the areas of computer systems and software which utilize them for problem solving. Sophisticated and accurate numerical algorithms are devised routinely that are capable of handling complex computational problems. Experimental test facilities capable of addressing complicated high-speed flow problems are still scarce because they are too



expensive to build and sophisticated measurements techniques appropriate for such problems, such as the non-intrusive laser, are still in the development stage. As a result, CFD has become a vital tool in the flow problem solution.

In high speed flows, any adjustment of chemical composition or thermodynamic equilibrium to a change in local environment requires certain time. This is because the redistribution of chemical species and internal energies require certain number of molecular collisions, and hence a certain characteristic time. Chemical non-equilibrium occurs when the characteristic time for the chemical reactions to reach local equilibrium is of the same order as the characteristic time of the fluid flow. Similarly, thermal non-equilibrium occurs when the characteristic time for translation and various internal energy modes to reach local equilibrium is of the same order as the characteristic time of the fluid flow. Since chemical and thermal changes are the results of collisions between the constituent particles, non-equilibrium effects prevail in high-speed flows in low-density air.

In chemical non-equilibrium flows the mass conservation equation is applied to each of the constituent species in the gas mixture. Therefore, the overall mass conservation equation is replaced by as many species conservation equations as the number of chemical species considered. The assumption of thermal non-equilibrium introduces additional energy conservation equations – one for every additional energy mode. Thus, the number of governing equations for non-equilibrium flow is much bigger compared to those for perfect gas flow. A complete set of governing equations for non-equilibrium flow may be found in [17-18].

The problems of chemical non-equilibrium in the shock layers over vehicles flying at high speeds and high altitudes in the Earth's atmosphere have been discussed by several investigators [19-22]. Most of the existing computer codes for calculating the non-equilibrium reacting flow use the one-temperature model, which assumes that all of the internal energy modes of the gaseous species are in equilibrium with the translational mode [21-22]. It has been pointed out that such a one-temperature description of the flow leads to a substantial overestimation of the rate of equilibrium because of the elevated vibrational temperature [20]. A three-temperature chemical-kinetic model has been proposed by [23] to describe the relaxation phenomena correctly in such a flight regime. However, the model is quite complex and requires many chemical rate parameters which are not yet known. As a compromise between the three-temperature and the conventional one-temperature model, a two-temperature chemical-kinetic model has been developed ([24-25]), which is designated herein as the TTV model. The TTV model uses one temperature  $T$  to characterize both the translational energy of the atoms and molecules and the rotational energy of the molecules, and another temperature  $T_v$  to characterize the vibrational energy of the molecules, translational energy of the electrons, and electronic excitation energy of atoms and molecules. The model has been applied to compute the thermodynamic properties behind a normal shock wave in a flow through a constant-area duct [24-25]. Radiation emission from the non-equilibrium flow has been calculated using the Non-equilibrium Air Radiation (NEQAIR) program [26-27]. The flow and the radiation computations have been packaged into a single computer program, the Shock-Tube Radiation Program (STRAP) [25].

In the present work, a study involving a spectral method to solve the reactive Euler and Navier-Stokes equations is performed. The Euler and Navier-Stokes equations, in conservative and finite volume contexts, employing structured spatial discretization, on a condition of thermochemical non-equilibrium, are studied. The spectral method presented in this work employs collocation points and variants of Chebyshev and Legendre interpolation functions are analyzed. High-order studies are accomplished to verify the accuracy of the spectral method. The "hot gas" hypersonic flows around a blunt body, around a double ellipse, and around a reentry capsule in two-dimensions are simulated. The [28-29] flux vector splitting algorithms are applied to execute the numerical experiments. The Euler backward integration method is employed to march the schemes in time. The convergence process is accelerated to steady state condition through a spatially variable time step procedure, which has proved effective gains in terms of computational acceleration [30-31]. The reactive simulations involve Earth atmosphere chemical model of five species and seventeen reactions, based on the [32] model. N, O,  $N_2$ ,  $O_2$ , and NO species are used to accomplish the numerical comparisons. The results have indicated that the Chebyshev collocation point variants are more accurate in terms of stagnation pressure estimations. Errors inferior to 16.16% were found for this parameter in the inviscid case, while inferior to 11.55% for the viscous case. The Legendre collocation point variants are more accurate in terms of the lift coefficient estimations.



## 2. Spectral Method

Two classes of techniques for spectral discretization are referred to as tau and collocation methods [33]. The latter technique is used here. In this scheme, the approximation series is determined by satisfying the differential equation exactly at a set of distinct collocation points. The locations of these points in the domain are linked to the choice of basis function. In this study, arbitrary collocation points are implemented. The collocation method is used here since enforcement of boundary conditions and evaluations of nonlinear terms are straightforward. Additionally, some accuracy advantage is seen in the collocation method over the tau method for a number of problems [33]. The series expansion for a function  $Q(x)$  may be represented as

$$Q_N(x) = \sum_{n=0}^N \hat{Q}_n B_n(x), \quad (1)$$

Where  $B_n(x)$  are the basis functions and  $N$  is the total number of nodes employed in the interpolation process (It is also the order of accuracy of the spectral method). The coefficients  $\hat{Q}_n$  are often termed the spectrum of  $Q_N(x)$ . One common technique used to evaluate the spectrum is to consider Eq. (1) as an interpolation series representing  $Q(x)$ . The interpolation “nodes” of such series are the collocation points of the method. For a scheme based on Chebyshev collocation, the basis functions are:

$$B_n(x) = T_n(x) = 2xP_{n-1}(x) - P_{n-2}(x), \quad n \geq 2, \quad (2)$$

with:  $P_0(x) = 1$  and  $P_1(x) = x$ . The Chebyshev-Gauss-Lobatto standard collocation points are

$$x_l = \cos\left(\frac{\pi l}{N}\right), \quad l = 0, 1, \dots, N. \quad (3)$$

The Chebyshev collocation points result from a simple change of variables, which relates the Chebyshev interpolation series to a Fourier cosine series [33]. To evaluate the  $\hat{Q}_n$ , the inverse relation is required. This is

$$\hat{Q}_n = \hat{c}_n \sum_{l=0}^N w_l B_n(x_l) Q_{l,j}, \quad n = 0, 1, \dots, N, \quad (4)$$

With  $w_l$  being a normalized weighting function and  $\hat{c}_n$  a constant. These variables assume the following expressions to a Chebyshev-Gauss-Lobatto interpolation:

$$\hat{c}_n = \frac{2}{N\bar{c}_n}, \quad \text{where: } \bar{c}_n = \begin{cases} 2, & n = 0 \text{ or } N \\ 1, & 1 < n < N-1 \end{cases}; \quad \text{and } w_l = \frac{1}{\bar{c}_l}. \quad (5)$$

Legendre collocation is based on using Legendre polynomials as the basis function in Eq. (1), e.g.,

$$B_n(x) = [(2n-1)xP_{n-1}(x) - (n-1)P_{n-2}(x)]/n, \quad n \geq 2, \quad (6)$$

where:  $P_0(x) = 1$  and  $P_1(x) = x$ . Interpolation via Legendre series cannot easily be related to trigonometric interpolation, so there is no simple expression to evaluate the  $\hat{Q}_n$  coefficients. Appeal must be made to the theory of numerical quadrature to form an approximation to the integrals which result from analytic Legendre interpolation [34]. Considering Eq. (4), the normalized weights and constant of the Legendre-Gauss-Lobatto collocation points are

$$w_l = \frac{1}{N(N+1)B_N^2(x_l)} \quad \text{and} \quad \hat{c}_n = \begin{cases} 2n+1, & n = 0, 1, \dots, N-1 \\ N, & n = N \end{cases}. \quad (7)$$

In this work, it was assumed that the Legendre-Gauss-Lobatto collocation points are the same as the Chebyshev-Gauss-Lobatto ones. It was also adopted the following collocation points and normalized weight for the Chebyshev-Gauss-Radau interpolation, based on the work of [35]:

$$x_l = \cos\left(\frac{2\pi l}{2N+1}\right), \quad (8)$$

$$w_l = \begin{cases} \frac{N}{2N+1}, & l = 0 \\ \frac{N}{N+1}, & \text{elsewhere} \end{cases}. \quad (9)$$



For the Legendre-Gauss-Radau interpolation, also based in [35], the collocation points are defined by Eq. (8) and the normalized weights are described by:

$$w_l = \begin{cases} \frac{1}{(N+1)^2}, & l = 0 \\ \frac{1}{2(N+1)^2} \times \frac{1-x_l}{B_N(x_l)}, & \text{elsewhere} \end{cases} \quad (10)$$

The same calculation to the vector of conserved variables  $Q$  is applied to the vector of flux  $C$ , to be defined in section 4.

Hence, we have two collocation point options and two normalized weight functions to be considered by the Chebyshev and the Legendre methods, namely: Chebyshev-Gauss-Radau, Chebyshev-Gauss-Lobatto, Legendre-Gauss-Radau and Legendre-Gauss-Lobatto.

### 3. Reactive Euler and Navier-Stokes Equations in 2D

As the Navier-Stokes equations tend to the Euler equations when high Reynolds number are employed, only the former equations are presented. The reactive Navier-Stokes equations in thermochemical non-equilibrium, where the rotational and vibrational contributions are considered, were implemented on conservative and finite volume contexts, in the two-dimensional space. In this case, these equations in integral and conservative forms can be expressed by:

$$\frac{\partial}{\partial t} \int_V Q dV + \int_S \vec{F} \cdot \vec{n} dS = \int_V S_{CV} dV, \text{ with: } \vec{F} = (E_e - E_v) \vec{i} + (F_e - F_v) \vec{j}, \quad (11)$$

where:  $Q$  is the vector of conserved variables,  $V$  is the volume of a computational cell,  $\vec{F}$  is the complete flux vector,  $\vec{n}$  is the unity vector normal to the flux face,  $S$  is the flux area,  $S_{CV}$  is the chemical and vibrational source term,  $E_e$  and  $F_e$  are the convective flux vectors or the Euler flux vectors in the  $x$  and  $y$  directions, respectively, and  $E_v$  and  $F_v$  are the viscous flux vectors in the  $x$  and  $y$  directions, respectively. The  $\vec{i}$  and  $\vec{j}$  unity vectors define the Cartesian coordinate system. Nine (9) conservation equations are solved: one of general mass conservation, two of linear momentum conservation, one of total energy, four of species mass conservation, and one of the vibrational internal energy of the molecules. Therefore, one of the species is absent of the iterative process. The CFD literature recommends that the species of biggest mass fraction of the gaseous mixture should be omitted, aiming to result in a minor numerical accumulation error. To the present study, in which is chosen a chemical model to the air composed of five (5) chemical species ( $N$ ,  $O$ ,  $N_2$ ,  $O_2$ , and  $NO$ ) and seventeen chemical reactions to the [32] model, this species can be the  $N_2$  or the  $O_2$ . To this work, the  $N_2$  was chosen. The vectors  $Q$ ,  $E_e$ ,  $F_e$ ,  $E_v$ ,  $F_v$ , and  $S_{CV}$  can, hence, be defined as follows:

$$Q = \begin{Bmatrix} \rho \\ \rho u \\ \rho v \\ e \\ \rho_1 \\ \rho_2 \\ \rho_4 \\ \rho_5 \\ \rho e_v \end{Bmatrix}, E_e = \begin{Bmatrix} \rho u \\ \rho u^2 + p \\ \rho uv \\ \rho Hu \\ \rho_1 u \\ \rho_2 u \\ \rho_4 u \\ \rho_5 u \\ \rho e_{v,u} \end{Bmatrix}, F_e = \begin{Bmatrix} \rho v \\ \rho uv \\ \rho v^2 + p \\ \rho Hv \\ \rho_1 v \\ \rho_2 v \\ \rho_4 v \\ \rho_5 v \\ \rho e_{v,v} \end{Bmatrix}, E_v = \frac{1}{Re} \begin{Bmatrix} 0 \\ \tau_{xx} \\ \tau_{xy} \\ f_x - \phi_x \\ -\rho_1 v_{1x} \\ -\rho_2 v_{2x} \\ -\rho_4 v_{4x} \\ -\rho_5 v_{5x} \\ q_{v,x} - \phi_{v,x} \end{Bmatrix}, F_v = \frac{1}{Re} \begin{Bmatrix} 0 \\ \tau_{xy} \\ \tau_{yy} \\ f_y - \phi_y \\ -\rho_1 v_{1y} \\ -\rho_2 v_{2y} \\ -\rho_4 v_{4y} \\ -\rho_5 v_{5y} \\ q_{v,y} - \phi_{v,y} \end{Bmatrix}; \quad (12)$$

$$S_{CV} = \left\{ 0 \quad 0 \quad 0 \quad 0 \quad \dot{\omega}_1 \quad \dot{\omega}_2 \quad \dot{\omega}_4 \quad \dot{\omega}_5 \quad \sum_{s=\text{mol}} \rho_s (e_{v,s}^* - e_{v,s}) / \tau_s + \sum_{s=\text{mol}} \dot{\omega}_s e_{v,s} \right\}^T; \quad (13)$$



in which:  $\rho$  is the mixture density;  $u$  and  $v$  are Cartesian components of the velocity vector in the  $x$  and  $y$  directions, respectively;  $e$  is the fluid total energy;  $H$  is the total enthalpy;  $\rho_1, \rho_2, \rho_4,$  and  $\rho_5$  are densities of the N, O, O<sub>2</sub>, and NO, respectively;  $e_v$  is the sum of the vibrational energy of the molecules; the  $\tau$ 's are the components of the viscous stress tensor;  $f_x$  and  $f_y$  are viscous work and Fourier heat flux functions;  $\rho_s v_{sx}$  and  $\rho_s v_{sy}$  represent the species diffusion flux, defined by the Fick law;  $\phi_x$  and  $\phi_y$  are the terms of mixture diffusion;  $\phi_{v,x}$  and  $\phi_{v,y}$  are the terms of molecular diffusion calculated at the vibrational temperature;  $\dot{\omega}_s$  is the chemical source term of each species equation, defined by the law of mass action;  $e_v^*$  is the molecular-vibrational-internal energy calculated with the translational/rotational temperature;  $\tau_s$  is the translational-vibrational characteristic relaxation time of each molecule;  $q_{v,x}$  and  $q_{v,y}$  are the vibrational Fourier heat flux components in the  $x$  and  $y$  directions, respectively; and  $Re$  is the laminar Reynolds number.

The viscous stresses, in N/m<sup>2</sup>, are determined, according to a Newtonian fluid model, by:

$$\begin{aligned}\tau_{xx} &= [2\mu_m \partial u / \partial x - 2/3 \mu_m (\partial u / \partial x + \partial v / \partial y)] ; \\ \tau_{xy} &= \mu_m (\partial u / \partial y + \partial v / \partial x) ; \\ \tau_{yy} &= [2\mu_m (\partial v / \partial y) - 2/3 \mu_m (\partial u / \partial x + \partial v / \partial y)] ,\end{aligned}\quad (14)$$

where  $\mu_m$  is the molecular viscosity. Expressions to  $f_x$  and  $f_y$  are given below:

$$f_x = \tau_{xx} u + \tau_{xy} v + q_x + q_{v,x} ; \quad (15)$$

$$f_y = \tau_{xy} u + \tau_{yy} v + q_y + q_{v,y} , \quad (16)$$

where  $q_x$  and  $q_y$  are the Fourier heat flux components and are given by:

$$q_x = k \frac{\partial T}{\partial x} \text{ and } q_y = k \frac{\partial T}{\partial y} . \quad (17)$$

where:  $k$  is the thermal conductivity due to translation and rotation. The  $q_{v,x}$  and  $q_{v,y}$  are the vibrational heat flux components and are given by:

$$q_{v,x} = k_v \partial T_v / \partial x \text{ and } q_{v,y} = k_v \partial T_v / \partial y , \quad (18)$$

with  $k_v$  being the vibrational thermal conductivity and  $T_v$  is the vibrational temperature, what characterizes this model as of two temperatures: translational/rotational and vibrational. The terms of species diffusion, defined by the Fick law, to a condition of thermal non-equilibrium, are determined by [36]:

$$\rho_s v_{sx} = -\rho D_s \frac{\partial Y_{MF,s}}{\partial x} \text{ and } \rho_s v_{sy} = -\rho D_s \frac{\partial Y_{MF,s}}{\partial y} , \quad (19)$$

with "s" referent to a given species,  $Y_{MF,s}$  being the molar fraction of the species, defined as:

$$Y_{MF,s} = \frac{\rho_s / M_s}{\sum_{k=1}^{ns} \rho_k / M_k} \quad (20)$$

and  $D_s$  is the species-effective-diffusion coefficient. "ns" is the number of species. The diffusion terms  $\phi_x$  and  $\phi_y$  which appear in the energy equation are defined by [32]:

$$\phi_x = \sum_{s=1}^{ns} \rho_s v_{sx} h_s \text{ and } \phi_y = \sum_{s=1}^{ns} \rho_s v_{sy} h_s , \quad (21)$$

being  $h_s$  the specific enthalpy (sensible) of the chemical species "s". The molecular diffusion terms calculated at the vibrational temperature,  $\phi_{v,x}$  and  $\phi_{v,y}$ , which appear in the vibrational-internal-energy equation are defined by [36]:

$$\phi_{v,x} = \sum_{s=mol} \rho_s v_{sx} h_{v,s} \text{ and } \phi_{v,y} = \sum_{s=mol} \rho_s v_{sy} h_{v,s} , \quad (22)$$



with  $h_{v,s}$  being the specific enthalpy (sensible) of the chemical species “s” calculated at the vibrational temperature  $T_v$ . The sum of Eq. (13), as also those present in Eq. (22), considers only the molecules of the system, namely:  $N_2$ ,  $O_2$ , and  $NO$ . The laminar Reynolds number is estimated by:

$$Re = \frac{\rho_{char} V_{initial} L_{char}}{\mu_{m,char}}, \quad (23)$$

With “char” representing characteristic or freestream properties,  $\rho_{char}$  is the characteristic density,  $V_{initial}$  is the flow initial velocity,  $L_{char}$  is a characteristic configuration length, and  $\mu_{m,char}$  is a characteristic molecular viscosity. For details of the chemical model, the calculation of thermodynamic and transport properties see [37-38].

#### 4. Numerical Schemes

Considering the two-dimensional and structured case, the flux vector splitting algorithms follow that described in [28-29, 37-38]. The speed of sound is defined by the following expression:

$$a = \sqrt{(\beta + 1) \frac{p}{\rho}}, \quad (24)$$

where  $\beta$  is a parameter to be defined, calculated at each interaction.

The system is solved in three parts separately, according to [39]. The first part takes into account the dynamic part, which considers the Navier-Stokes equations, the second one takes into account the chemical part involving the chemical contributions, and finally, the third part considers only the vibrational contribution. Hence, the discrete-dynamic-convective flux, which solves the dynamic part, is given by:

$$R_{i+1/2,j} = |S|_{i+1/2,j} \left\{ \frac{1}{2} M_{i+1/2,j} \left[ \begin{pmatrix} \rho a \\ \rho a u \\ \rho a v \\ \rho a H \end{pmatrix}_L + \begin{pmatrix} \rho a \\ \rho a u \\ \rho a v \\ \rho a H \end{pmatrix}_R \right] - \frac{1}{2} \phi_{i+1/2,j} \left[ \begin{pmatrix} \rho a \\ \rho a u \\ \rho a v \\ \rho a H \end{pmatrix}_R - \begin{pmatrix} \rho a \\ \rho a u \\ \rho a v \\ \rho a H \end{pmatrix}_L \right] \right\} + \begin{pmatrix} 0 \\ S_x p \\ S_y p \\ 0 \end{pmatrix}_{i+1/2,j}, \quad (25)$$

the discrete-chemical-convective flux is defined by:

$$R_{i+1/2,j} = |S|_{i+1/2,j} \left\{ \frac{1}{2} M_{i+1/2,j} \left[ \begin{pmatrix} \rho_1 a \\ \rho_2 a \\ \rho_4 a \\ \rho_5 a \end{pmatrix}_L + \begin{pmatrix} \rho_1 a \\ \rho_2 a \\ \rho_4 a \\ \rho_5 a \end{pmatrix}_R \right] - \frac{1}{2} \phi_{i+1/2,j} \left[ \begin{pmatrix} \rho_1 a \\ \rho_2 a \\ \rho_4 a \\ \rho_5 a \end{pmatrix}_R - \begin{pmatrix} \rho_1 a \\ \rho_2 a \\ \rho_4 a \\ \rho_5 a \end{pmatrix}_L \right] \right\}, \quad (26)$$

and finally the discrete-vibrational-convective flux is given by:

$$R_{i+1/2,j} = |S|_{i+1/2,j} \left\{ \frac{1}{2} M_{i+1/2,j} [(\rho e_v a)_L + (\rho e_v a)_R] - \frac{1}{2} \phi_{i+1/2,j} [(\rho e_v a)_R - (\rho e_v a)_L] \right\}, \quad (27)$$

where:  $C$  is the sum of the fluxes at each interface, and  $S_{i+1/2,j} = [S_x \ S_y]^T_{i+1/2,j}$  defines the normal area vector for the surface  $(i+1/2,j)$ . The normal area components  $S_x$  and  $S_y$  to each flux interface are given in Tab. 1. Figure 1 exhibits the computational cell adopted for the simulations, as well its respective nodes and flux interfaces.

The same definitions presented in [28-29, 37-38] are valid to these algorithms. The definition of the dissipation term  $\phi$  determines the particular formulation of the convective fluxes. The choice below corresponds to the [28] scheme, according to [40]:



$$\phi_{i+1/2,j} = \phi_{i+1/2,j}^{VL} = \begin{cases} |M_{i+1/2,j}|, & \text{if } |M_{i+1/2,j}| \geq 1; \\ |M_{i+1/2,j}| + 0.5(M_R - 1)^2, & \text{if } 0 \leq M_{i+1/2,j} < 1; \\ |M_{i+1/2,j}| + 0.5(M_L + 1)^2, & \text{if } -1 < M_{i+1/2,j} \leq 0. \end{cases} \quad (28)$$

and the [29] scheme is obtained by, according to [40]:

$$\phi_{i+1/2,j} = \phi_{i+1/2,j}^{LS} = |M_{i+1/2,j}|. \quad (29)$$

Both schemes are first-order accurate in space and in time. The high-order spatial accuracy is obtained, in the current study, by the spectral method.

The viscous formulation follows that of [41], which adopts the Green theorem to calculate primitive variable gradients. The viscous gradient at the flux interface are obtained by arithmetical average between cell (i,j) and its neighbors. As was done with the convective terms, there is a need to separate the viscous flux in three parts: dynamic viscous flux, chemical viscous flux, and vibrational viscous flux. The dynamic part corresponds to the first four equations of the Navier-Stokes, the chemical part corresponds to the four equations immediately below the energy equation, and the vibrational part corresponds to the equation that follows the last chemical one. The resultant ordinary differential equation system can be written as:

$$V_{i,j} dQ_{i,j}/dt = -(R_{i,j-1/2} + R_{i+1/2,j} + R_{i,j+1/2} + R_{i-1/2,j}) = -C_{i,j}, \quad (30)$$

where the cell volume is given by:

$$V_{i,j} = 0.5 \left[ (x_{i,j} - x_{i+1,j})y_{i+1,j+1} + (x_{i+1,j} - x_{i+1,j+1})y_{i,j} + (x_{i+1,j+1} - x_{i,j})y_{i+1,j} \right] + 0.5 \left[ (x_{i,j} - x_{i+1,j+1})y_{i,j+1} + (x_{i+1,j+1} - x_{i,j+1})y_{i,j} + (x_{i,j+1} - x_{i,j})y_{i+1,j+1} \right]. \quad (31)$$

In the present study, the Euler backward method was employed to march the scheme in time. This method is first-order accurate in time, to the three types of complete flux. To the convective dynamic component, this method can be represented in general form by:

$$Q_{i,j}^{(n+1)} = Q_{i,j}^{(n)} - (\Delta t_{i,j}/V_{i,j}) \times C(Q_{i,j}^{(n)}), \quad (32)$$

to the convective chemical part, it can be represented in general form by:

$$Q_{i,j}^{(n+1)} = Q_{i,j}^{(n)} - \Delta t_{i,j} \times [C(Q_{i,j}^{(n)})/V_{i,j} - S_C(Q_{i,j}^{(n)})], \quad (33)$$

where the chemical source term  $S_C$  is calculated with the temperature  $T_{rc}$  (reaction rate controlling temperature, see [37-38]). Finally, to the convective vibrational component:

$$Q_{i,j}^{(n+1)} = Q_{i,j}^{(n)} - \Delta t_{i,j} \times [C(Q_{i,j}^{(n)})/V_{i,j} - S_V(Q_{i,j}^{(n)})], \quad (34)$$

in which:

$$S_V = \sum_{s=mol} q_{T-V,s} + \sum_{s=mol} S_{C,s} e_{v,s}, \quad (35)$$

Where  $q_{T-V}$  is the heat flux due to translational-vibrational relaxation, defined in Eq. (13) and in [37-38].

### 5. Spatially Variable Time Step

The spatially variable time step has proved efficient gains in terms of convergence acceleration, as verified by [30-31]. Initially, the parameter  $\sigma$  is determined, where:

$$\sigma_s = \frac{c_s}{M_s} \text{ and } \sigma = \sum_{s=1}^{ns} \sigma_s, \quad (36)$$

With  $c_s$  being the mass fraction, and  $M_s$  the molecular weight. The total specific heat at constant volume due to translation is defined as:

$$c_{V,T} = \sum_{s=1}^{ns} \sigma_s c_{V,T,s}, \quad (37)$$





where, for each gas constituent of the five (5) species chemical model, the specific heat at constant volume, based on the kinetic theory of gases [42], is defined by

$$c_{v,T,N} = \frac{3}{2}R_N, \quad c_{v,T,O} = \frac{3}{2}R_O, \quad c_{v,T,N_2} = \frac{5}{2}R_{N_2}, \quad c_{v,T,O_2} = \frac{5}{2}R_{O_2}, \quad \text{and} \quad c_{v,T,NO} = \frac{5}{2}R_{NO}, \quad (38)$$

Being  $R_s$  the specific gas constant. The total pressure of the gaseous mixture is determined by Dalton law, which indicates that the total pressure of the gas is the sum of the partial pressure of each constituent gas, resulting in:

$$p_s = c_s \rho R_s T \quad \text{and} \quad p = \sum_{s=1}^{ns} p_s. \quad (39)$$

The speed of sound to a reactive mixture can be determined by Eq. (24), where  $\beta = \frac{R_{univ}\sigma}{c_{v,T}}$ , with  $R_{univ} = 1.987$

cal/(g-mol.K). Finally, the spatially variable time step is defined from the CFL (Courant-Friedrichs-Lewis) definition:

$$\Delta t_{i,j} = \frac{CFL \Delta s_{i,j}}{\sqrt{u_{i,j}^2 + v_{i,j}^2 + a_{i,j}}}, \quad (40)$$

where  $\Delta s_{i,j}$  is the characteristic length of each cell (defined between the minimum cell side length and the minimum centroid distance between each cell and its neighbors).

## 6. Dimensionless Scales, Initial and Boundary Conditions

### 6.1. Dimensionless Scales

The dimensionless scales employed to the reactive equations consisted in:  $R_s$  is dimensionless by  $a_{char}$ , where  $a_{char} = \sqrt{\gamma p_{char} / \rho_{char}}$ ;  $c_v$  is dimensionless by  $a_{char}$ ;  $h_s$  and  $\Delta h_s^0$  are dimensionless by  $a_{char}^2$ ;  $T$  and  $T_v$ , translational/rotational temperature and vibrational temperature, respectively, are dimensionless by  $a_{char}$ ;  $\rho_s$  and  $\rho$  are dimensionless by  $\rho_{char}$ ;  $u$  and  $v$  are dimensionless by  $a_{char}$ ;  $\mu$  is dimensionless by  $\mu_{char}$ ;  $D$ , diffusion coefficient, dimensionless by  $a_{char}^2 dt_{char}$ , where  $dt_{char}$  is the minimum time step calculated in the computational domain at the first iteration;  $\dot{\omega}$  is dimensionless by  $(\rho_{char} / dt_{char}) \times 10^{-3}$ ;  $e_v$  is dimensionless by  $a_{char}^2$ ;  $e$  and  $p$  are dimensionless by  $\rho_{char} a_{char}^2$ ;  $\tau_s$ , relaxation time, is dimensionless by  $dt_{char}$ . The characteristic physical properties are defined in [43].

### 6.2. Initial Condition

The initial conditions to the blunt body, to the double ellipse, and to the reentry capsule problems, for a five species chemical model, are presented in Tabs. 2-4. The Reynolds number is obtained from data of [43].

### 6.3. Boundary Conditions

The boundary conditions are basically of four types: solid wall, entrance, exit, and continuity. These conditions are implemented with the help of ghost cells.

**Wall condition.** In the inviscid case, this condition imposes the flow tangency at the solid wall. This condition is satisfied considering the wall tangent velocity component of the ghost volume as equals to the respective velocity component of its real neighbor cell. At the same way, the wall normal velocity component of the ghost cell is equaled in value, but with opposite signal, to the respective velocity component of the real neighbor cell. It results in:

$$n_x = \Delta y / \sqrt{\Delta x^2 + \Delta y^2}; \quad \text{and} \quad n_y = -\Delta x / \sqrt{\Delta x^2 + \Delta y^2}; \quad (41)$$

where, for the  $(i+1/2,j)$  interface:

$$\Delta x = x_{i+1,j+1} - x_{i+1,j}; \quad \text{and} \quad \Delta y = y_{i+1,j+1} - y_{i+1,j}. \quad (42)$$



Hence, the ghost cell velocity components are written as:

$$\mathbf{u}_g = (n_y^2 - n_x^2)\mathbf{u}_r - (2n_x n_y)\mathbf{v}_r; \quad \text{and} \quad \mathbf{v}_g = -(2n_x n_y)\mathbf{u}_r + (n_x^2 - n_y^2)\mathbf{v}_r. \quad (43)$$

with “g” related with ghost cell and “r” related with real cell. To the viscous case, the boundary condition imposes that the ghost cell velocity components be equal to the real cell velocity components, with the negative signal:

$$\mathbf{u}_g = -\mathbf{u}_r \quad \text{and} \quad \mathbf{v}_g = -\mathbf{v}_r. \quad (44)$$

The normal pressure gradient of the fluid at the wall is assumed to be equal to zero according to a boundary-layer like condition. The same hypothesis is applied for the normal temperature gradient at the wall, assuming an adiabatic wall. From the above considerations, density and translational/rotational temperature are extrapolated from the respective values of its real neighbor volume (zero order extrapolation). The total vibrational internal energy is also extrapolated.

With the mixture species mass fractions and with the values of the respective specific heats at constant volume, it is possible to obtain the mixture specific heat at constant volume. The mixture formation enthalpy is extrapolated from the real cell. The mixture total energy to the ghost cell is calculated by:

$$e_g = \rho_g \left[ c_{v,mixt,g} (T_{tr,g} - T_{REF}) + \Delta h_{mixt,g}^0 + e_{v,g} + 0.5(u_g^2 + v_g^2) \right], \quad (45)$$

Where  $c_{v,mixt,g}$ ,  $T_{REF}$ ,  $e_{v,g}$  are defined in [37-38]. To the species density, the non-catalytic condition is imposed, what corresponds to zero order extrapolation from the real cell.

**Entrance condition.** It is divided in two flow regimes:

- (a) Subsonic flow: Three properties are specified and one extrapolated in the boundary conditions of the dynamic part of the [28-29] numerical schemes. This approach is based on information propagation analysis along characteristic directions in the calculation domain [44]. In other words, for subsonic flow, three characteristics propagate information pointing into the computational domain. Thus three flow properties must be fixed at the inlet plane. Just one characteristic line allows information to travel upstream. So, one flow variable must be extrapolated from the interior grid to the inlet boundary. The total energy was the extrapolated variable from the real neighbor volume, for the studied problems. Density and velocity components adopted values of initial flow. To the chemical part, four information propagate upstream because it is assumed that all four equations are conducted by the eigenvalue “(q<sub>n</sub>-a)”. In the subsonic flow, all eigenvalues are negative and the information should be extrapolated. In the same reasoning to the chemical boundary conditions, the vibrational-internal-energy equation is dictated by the “(q<sub>n</sub>-a)” eigenvalue and, in the subsonic region, its value is negative. Hence, the vibrational internal energy should be extrapolated.
- (b) Supersonic flow: In this case no information travels upstream; therefore all variables are fixed with their initial values.

**Exit condition.** It is also divided in two flow regimes:

- (a) Subsonic flow: Three characteristics propagate information outward the computational domain. Hence, the associated variables should be extrapolated from interior information. The characteristic direction associated to the “(q<sub>normal</sub>-a)” velocity should be specified because it points inward to the computational domain [44]. In this case, the ghost volume total energy is specified from its initial value. Density and velocity components are extrapolated. To the chemical part, the eigenvalue “(q<sub>n</sub>-a)” is again negative and the characteristics are always flowing into the computational domain. Hence, the four chemical species under study should have their densities fixed by their initial values. In the same reasoning, the internal vibrational energy should have its value prescribed by its initial value due to the eigenvalue “(q<sub>n</sub>-a)” be negative.
- (b) Supersonic flow: All variables are extrapolated from interior grid cells, as no flow information can make its way upstream. In other words, nothing can be fixed.

**Continuity condition.** This condition imposes continuity of the flow at the trailing edge of the reentry capsule configuration. This is done considering the Kutta condition in this region. In terms of numerical implementation,



it is obtained considering the vector of conserved variables above the wake as equal to the vector of conserved variables below the wake.

## 7. Physical Problems

Three physical problems were solved in this work, namely: blunt body, double ellipse, and reentry capsule. The first problem considers the geometry of a blunt body with 1.0 m of nose ratio and parallel rectilinear walls. The far field is located at 20.0 times the nose ratio in relation to the configuration nose. A mesh composed of 2,548 rectangular cells and 2,650 nodes was studied for the inviscid case, with an exponential stretching of 5.0% for the viscous case. This mesh is equivalent in finite differences to a one of 53x50 points. Figure 2 shows the detail of the geometry and Figs. 3 and 4 exhibit the inviscid and viscous meshes.

The double ellipse problem is the second under study. The mesh is composed of 4,116 rectangular cells and 4,250 nodes, with an exponential stretching of 5.0% for the viscous case, and far field located at 20.0 unities. This mesh is equivalent in finite differences to a one of 85x50 points. Figure 5 shows the double ellipse geometry and Figs. 6 and 7 exhibit the inviscid and viscous meshes.

The third problem is the geometry of the reentry capsule. Details of the configuration are presented in Fig. 8. The far field is located also at 20.0 unities. A mesh of 3,136 rectangular cells and 3,250 nodes was used for the inviscid case, whereas with an exponential stretching of 5.0% was used for the viscous simulations. This mesh is equivalent in finite differences to a one of 65x50 points. Figures 9 and 10 show the inviscid and viscous meshes.

## 8. Results

Tests were performed in a Core i7 processor of 2.8GHz and 6.0Gbytes of RAM microcomputer, in a Windows 7.0 environment. Three (3) orders of reduction of the maximum residual in the field were considered to obtain a converged solution. The residual was defined as the value of the discretized conservation equation. In the dynamic part of the [28-29] schemes, such definition results in:

$$\text{Residual} = -\Delta t_{i,j} / V_{i,j} \times C_{i,j}. \quad (46)$$

The attack angle was adopted equal to zero. In this work, the inviscid results were obtained for a 5<sup>th</sup> order of accuracy of the spectral method, whereas the viscous solutions were obtained for an 8<sup>th</sup> order of accuracy of the spectral method. For a matter of simplicity, the following abbreviations were used: [28] scheme = VL, [29] scheme = LS, Chebyshev-Gauss-Radau = CGR, Chebyshev-Gauss-Lobatto = CGL, Legendre-Gauss-Radau = LGR, and Legendre-Gauss-Lobatto = LGL.

### 8.1. Blunt Body Problem

**Inviscid case.** Figures 11 to 14 exhibit the pressure and temperature contours obtained by the VL and LS schemes as using the CGR collocation points. The VL algorithm captures a more intense shock than the LS scheme, as can be seen by the pressure contours. Good symmetry and homogenous properties are observed in the pressure and in the translational/rotational temperature contours. No pre-shock oscillations are observed. The maximum temperature at the configuration nose is 9,379.84K, obtained by the LS scheme.

Figures 15 to 18 show the pressure and translational/rotational temperature contours generated by the VL and LS schemes as using CGL collocation points. The maximum pressure is obtained by the LS algorithm, being inferior to that observed in the CGR case. Some pressure oscillations are observed close to the shock wave in the LS' solution. The temperature contours presents good symmetry properties. The maximum temperature reaches the value of 8,519.27K and is captured by the VL scheme. The contours are free of oscillations.

Figures 19 to 22 present the pressure and translational/rotational temperature contours calculated by the VL and LS schemes when using the LGR collocation points. The pressure peaks of both solutions are smaller than those obtained in the Chebyshev variants. No pressure oscillations are observed and good symmetry properties are verified. The maximum temperature peak is 8,885.07K, obtained again by the VL scheme. Good symmetry properties are also observed in both temperature contours.

Figures 23 to 26 exhibit the pressure and temperature contours obtained by the VL and LS algorithms when using the LGL collocation points. The pressure peaks are still low. Good symmetry and homogeneous properties are observed and the shock wave is well captured. The temperature contours present also good symmetry



properties, free of oscillations. The maximum temperature is obtained by the VL scheme with a value of 8,935.64K.

**Viscous case.** Figures 27 to 30 present the pressure and temperature contours generated by the VL and LS schemes as using CGR collocation points. The pressure peaks are close to the theoretical stagnation pressure value, with LS scheme being the closest. Good symmetry properties are observed and no pre-shock oscillations are observed. The maximum temperature is calculated with the LS scheme, reaching the mark of 8,702.43K. Good symmetry properties are verified in the temperature field. Note that the heat transfer is better captured by the VL scheme, as can be seen by the contours of temperature close to the configuration wall. The correct transport of properties like viscosity and thermal conduction are qualitatively confirmed.

Figures 31 to 34 show the pressure and translational/rotational temperature contours calculated by the VL and LS algorithms when using CGL collocation points. Again the LS' pressure peak is very close to the theoretical value of stagnation pressure (see Table 5). The shock wave is well captured by both schemes. Figures 33 and 34 show the translational/rotational temperature contours and the good transport of viscosity and thermal conduction is noted in the VL solution. The maximum temperature is 8,785.93K and is again obtained by the VL scheme; in other words, the VL scheme is being more conservative than the LS scheme.

Figures 35 to 38 exhibit the pressure and temperature contours obtained by the VL and LS algorithms as using the LGR collocation points. Both pressure contours are very similar in qualitative terms, although the pressure peaks are very low. Good symmetry properties are observed in both solutions, free of pre-shock oscillations. Figures 37 and 38 exhibit the temperature contours calculated by the VL and LS schemes. The temperature field of VL algorithm is more intense than that of the LS scheme, reaching a maximum of 9,240.20K. Good symmetry and homogenous properties are observed in both figures.

Figures 39 to 42 present the pressure and translational/rotational temperature contours calculated by the VL and LS algorithms when using the LGL collocation points. Both pressures are reduced in relation to the theoretical stagnation pressure value. Both solutions present good symmetry and homogenous properties, free of oscillations. The shock waves are well captured and the transport of properties is well highlighted in the VL's temperature contours. The maximum temperature is obtained by the VL scheme and reaches the value of 9,220.17K. The Legendre solutions present in general higher values to the stagnation temperature than the Chebyshev solutions. It seems that Chebyshev variants dominate the pressure field, whereas the Legendre variants dominate the temperature field.

## 8.2. Double Ellipse Problem

**Inviscid case.** In this problem, only the VL scheme converged in the numerical simulations. Figures 43 to 50 show pressure and temperature contours generated by the VL algorithms as using the CGR, CGL, LGR, and LGL collocation points. Comparing with the theoretical stagnation pressure value, the best result is due to CGR collocation points with an error of 6.33%. Good homogenous properties are observed in all solutions and the two shock waves are well captured by all spectral variants. Some oscillations in the temperature field are observed ahead of the configuration nose with the exception of the LGL solution. The maximum temperature in the field is captured by the LGL collocation points and reaches the value of 9,379.84K.

**Viscous case.** Again, only the VL scheme generated converged results. Figures 51 to 58 exhibit the pressure and temperature contours calculated with the VL schemes as using the CGR, CGL, LGR, and LGL variants of the proposed spectral method. The best value to the stagnation pressure is captured by the CGR collocation points, with an error of 3.01%. Good homogenous properties are observed in all solutions. Figures 52, 54, 56 and 58 exhibit the thermal boundary layer captured by all variants of the spectral method as using the VL scheme. The transport properties are well detected by the VL scheme. No temperature oscillations are observed in these figures. Both temperature fields calculated by the Legendre variants reach values above 10,150K and are the most intense fields in the double ellipse simulations.

## 8.3. Reentry Capsule Problem

**Inviscid case.** Figures 59 to 62 present the pressure and translational/rotational temperature contours obtained by the VL and LS schemes as using the CGR collocation points. Figures 59 and 60 present the pressure contours



and good symmetry and homogenous properties are verified. The stagnation pressure estimated by the LS scheme as using CGR collocation points is the best in comparison with the CGL, LGR, and LGL solutions, with an error of 3.04%. The Kutta condition was correctly implemented. There are qualitative differences in the pressure contours captured by both schemes. The solution of Figure 59 seems better to represent the normal shock. Figures 61 and 62 present the temperature contours and good symmetry properties are noted. Again, the normal shock seems better captured by the VL solution. The maximum temperature is captured by the VL scheme and has the value of 7,555.67K.

Figures 63 to 66 show the pressure and temperature contours generated by the VL and LS numerical algorithms when using the CGL collocation points. Good symmetry properties are observed in both solutions, free of pre-shock oscillations. The temperature contours are shown in Figs. 65 and 66 and both figures present good symmetry characteristics, without oscillations. The maximum temperature peak is obtained by the LS scheme and has the value of 7,866.45K.

Figures 67 to 70 exhibit the pressure and translational/rotational temperature contours calculated by the VL and LS algorithms as using the LGR collocation points. The values of stagnation pressure obtained by the numerical schemes are inferior to the theoretical value. As mentioned before, it seems that the Legendre variant behaves better for the temperature field and for the determination of the lift aerodynamic coefficient, as seen in Tabs. 8 and 9. Good symmetry properties are observed in all solutions and free of oscillations. The LS scheme again captures the maximum temperature in the field with a value of 8,063.48K.

Figures 71 to 74 show the pressure and translational/rotational temperature contours obtained by the VL and LS schemes as using the LGL collocation points. Both schemes capture correctly the normal shock wave ahead of the configuration nose. Moreover, the stagnation pressure values of both schemes are under-predicted in relation to the theoretical value. Good symmetry properties are observed. Good homogenous properties are verified in the temperature solutions. The trailing edge flow is well captured by the numerical schemes, emphasizing the correct implementation of the Kutta condition. The maximum temperature in the field is calculated by the LS algorithm and reaches the value of 8,125.17K.

**Viscous case.** Figures 75 and 76 exhibit the pressure and temperature contours calculated by the VL numerical scheme as using the CGR collocation points. The LS scheme did not converge for this variant. Good symmetry properties are observed. The dynamic and thermal shock waves are correctly captured by the VL algorithm. The stagnation temperature reaches the value of 8,196.63K.

Figures 77 to 80 show the pressure and translational/rotational temperature contours generated by the VL and LS schemes when using the CGL collocation points. The best result of the viscous case for the stagnation pressure was obtained by the LS scheme as using the CGL spectral variant with an error of 1.59%. Again, it seems that the Chebyshev variants present better behavior when applied to the dynamic part of the flow. Good symmetry properties are verified in the pressure and in the temperature fields. The maximum temperature peak is obtained by the LS scheme and has the value of 8,293.37K.

Figures 81 to 84 present the pressure and temperature contours obtained by the VL and LS numerical schemes as using the LGR collocation points. The stagnation pressure values generated by the VL and LS schemes are under-estimated in relation to the theoretical value. The contours are free of pre-shock oscillations and present good homogenous features. Figures 83 and 84 present the temperature contours. The normal thermal shock wave is well captured by the numerical algorithms. Good symmetry properties are observed and the wake is well captured by the numerical schemes, highlighting the correct implementation of the Kutta condition. The maximum temperature in the field is calculated by the VL schemes and has the value of 8,434.13K.

Figures 85 to 88 exhibit the pressure and temperature contours calculated by the VL and LS numerical algorithms when using the LGL collocation points. The stagnation pressure continues under-estimated. Good symmetry properties are verified. The temperature contours are free of oscillations, the wake is well captured by the numerical schemes, and good homogenous properties are noted. The normal thermal shock wave is well captured by the numerical schemes. The maximum temperature in the field is obtained by the LS scheme and reaches the value of 8,413.45K. Again the maximum temperature in the field was predominantly captured by the Legendre variants.



#### 8.4. Other Comparisons

Figure 89 shows the convergence history of the VL scheme for a 5<sup>th</sup> order spectral method using CGL for collocation points and for two ENO solutions also of 5<sup>th</sup> order using Newton and Hermite interpolation functions, to the blunt body inviscid case. The CGL collocation points were chosen because they provide the best convergence of the VL scheme for the inviscid case and 5<sup>th</sup> order of accuracy. The ENO procedure was implemented by the author and was used for numerical comparisons. To details of the implementation of the ENO procedure on a context of thermochemical non-equilibrium, the reader is encouraged to read [45-47]. As can be seen in Fig. 89, the spectral (CGL) method coupled with the VL scheme was the most efficient converging in 223 iterations, with a maximum CFL of 0.70. The ENO solutions were very inefficient compared with the spectral method. The maximum allowable CFL number employed in the ENO solutions was 0.01. Figure 90 compares the ENO solution of 5<sup>th</sup> order using Newton and Hermite interpolation functions, and the spectral (LGL) method, all of them coupled with the LS scheme. Again, the LGL collocation points were chosen due to provide the best convergence for the LS scheme in the inviscid case and 5<sup>th</sup> order of accuracy. In this case, the good convergence of the spectral (LGL) method was highlighted, converging in 263 iterations, whereas the ENO solutions converged in more than 10,000 iterations.

As conclusion, the correct implementation of the proposed spectral method led to an efficient high order scheme, converging in less than 300 iterations in the inviscid case, for the blunt body problem, when programmed coupled with the VL or LS schemes. The CGL and LGL variants of the spectral method were the most efficient in the studies performed by the author and ratified the fast convergence as expected.

#### 8.5. Quantitative Analysis

In order to perform a quantitative analysis, the present reactive results are compared to the perfect gas solutions. The stagnation pressures at the blunt body nose, at the double ellipse nose, and at the reentry capsule nose were evaluated assuming the perfect gas formulation. Such parameter calculated at this way is not the best comparison, but in the absence of practical reactive results, this constitutes the best available solution.

To calculate the stagnation pressure at the nose of these three configurations, [48] presents in its B Appendix values of the normal shock wave properties ahead of the configuration. The ratio  $pr_0/pr_\infty$  is estimated as function of the normal Mach number and the stagnation pressure  $pr_0$  can be determined from this parameter. Hence, Table 5 gives the theoretical stagnation pressure values obtained for the three configurations at the initial-normal-Mach number. The value of  $pr_\infty$  is determined by the following expression:

$$pr_\infty = \frac{pr_{\text{initial}}}{\rho_{\text{char}} \times a_{\text{char}}^2}, \quad (47)$$

where, for example, for the blunt body case,  $pr_{\text{initial}} = 687\text{N/m}^2$ ,  $\rho_{\text{char}} = 0.004\text{kg/m}^3$  and  $a_{\text{char}} = 317.024\text{m/s}$ . Considering these values, one concludes that  $pr_\infty = 1.709$  (non-dimensional). Using the ratio obtained from [48], the stagnation pressure ahead of the configuration nose is estimated as 170.87 unities. Tables 6 (inviscid case) and 7 (viscous case) compare values of the stagnation pressure obtained from the simulations with the theoretical values and show the percentage errors. As can be seen, the best results in the inviscid case are provided by the CGR collocation points, with an error of 1.94%, when coupled with the VL scheme, for the blunt body problem; by the CGR collocation points, with an error of 6.33%, when coupled with the VL scheme, for the double ellipse problem; and again by CGR collocation points, with an error of 3.04%, when coupled with the LS scheme, for the reentry capsule problem. For the viscous case, the CGL collocation points, with an error of 1.38%, coupled with the LS scheme, for the blunt body problem, was the best; with the CGR collocation points, with an error of 3.01%, coupled with the VL scheme, for the double ellipse problem, was the best; and with the CGL collocation points, with an error of 1.59%, coupled with the LS scheme, for the reentry capsule problem, was the best.

As the hypersonic flows around the blunt body and reentry capsule configurations were simulated with a zero value to the attack angle, a zero lift coefficient, due to geometry symmetry, is the expected value for this aerodynamic coefficient. Tables 8 (inviscid) and 9 (viscous) present an analysis of the lift aerodynamic coefficient, based only on pressure contribution, in this study. As can be observed, the best value to the lift



coefficient in the inviscid case is obtained by the LGR collocation points, coupled with the LS scheme, for the blunt body problem; and again by the LGR collocation points, coupled with the VL scheme, for the reentry capsule problem. In the viscous case, the best value to the lift coefficient is obtained by the LGR collocation points, coupled with the VL scheme, for the blunt body problem; and by the CGL collocation points, coupled with the VL scheme, for the reentry capsule problem.

### 8.6. Computational Performance

Tables 10 and 11 present the computational data of the VL and LS schemes for the blunt body, for the double ellipse, and for the reentry capsule problems in both inviscid and viscous cases. It shows the CFL number and the number of iterations to convergence for all studied cases in the current work. It can be verified that the best performance of the VL scheme in the inviscid case occurred when using the CGL collocation points, employing a CFL of 0.70, and converging in 223 iterations, in the blunt body problem, whereas in the viscous case occurred when using the LGR collocation points, employing a CFL of 0.30, and converging in 399 iterations, also in the blunt body problem. On the other hand, the best performance of the LS scheme in the inviscid case occurred when using the LGL collocation points, employing a CFL of 0.50, and converging in 263 iterations, in the blunt body problem, whereas in the viscous case occurred when using the LGR collocation points, employing a CFL of 0.50, and converging in 245 iterations, also in the blunt body problem.

As final conclusion, it is possible to highlight that, for the blunt body problem, the LS scheme in the viscous case using CGL collocation points had the best performance in estimating the stagnation pressure, and the lift aerodynamic coefficient was best estimated by the VL scheme as using the LGR collocation points; for the double ellipse problem, the VL scheme in the viscous case using CGR collocation points had the best performance in estimating the stagnation pressure; and finally, for the reentry capsule problem, the LS scheme in the viscous case using CGL collocation points had the best performance in estimating the stagnation pressure, and the lift aerodynamic coefficient was best estimated by the VL scheme as using the LGR collocation points. Moreover, the best performance of the numerical schemes, for the 5<sup>th</sup> order of accuracy, was due to the VL one, when using the CGL collocation points, employing a CFL of 0.70, and converging in 223 iterations, in the blunt body problem, whereas for the 8<sup>th</sup> order of accuracy, the best performance of the numerical schemes was due to the LS one, when using the LGR collocation points, employing a CFL of 0.50, and converging in 245 iterations, also in the blunt body problem.

Finally, to close this work, the computational cost of the numerical schemes using the several types of collocation points is presented in Tab. 12. For the inviscid case, the cheapest combination was the LS scheme using LGR collocation points with a cost of 0.0001344 sec/per-volume/per-iteration, whereas for the viscous case the cheapest was due to the VL scheme coupled with the LGL collocation points with a cost of 0.0002967 sec/per-volume/per-iteration.

**Table 1:** Values of  $S_x$  and  $S_y$ .

Surface	$S_x$	$S_y$
$i,j-1/2$	$(y_{i+1,j} - y_{i,j})$	$(x_{i,j} - x_{i+1,j})$
$i+1/2,j$	$(y_{i+1,j+1} - y_{i+1,j})$	$(x_{i+1,j} - x_{i+1,j+1})$
$i,j+1/2$	$(y_{i,j+1} - y_{i+1,j+1})$	$(x_{i+1,j+1} - x_{i,j+1})$
$i-1/2,j$	$(y_{i,j} - y_{i,j+1})$	$(x_{i,j+1} - x_{i,j})$

**Table 2:** Initial conditions to the blunt body problem

Property	Value
$M_{\text{initial}}$	8.78
$\rho_{\text{initial}}$	0.00326 kg/m <sup>3</sup>
$p_{\text{initial}}$	687 Pa
$U_{\text{initial}}$	4,776 m/s
$T_{\text{initial}}$	694 K



Altitude	40,000 m
$c_N$	$10^{-9}$
$c_O$	0.07955
$c_{O_2}$	0.13400
$c_{NO}$	0.05090
$L_{char}$	2.0 m
$Re_{char}$	$2.386 \times 10^6$

**Table 3:** Initial conditions to the double ellipse problem

Property	Value
$M_{initial}$	15.0
$\rho_{initial}$	0.00922 kg/m <sup>3</sup>
$p_{initial}$	794 Pa
$U_{initial}$	5,208 m/s
$T_{initial}$	300 K
Altitude	50,000 m
$c_N$	$10^{-9}$
$c_O$	0.07955
$c_{O_2}$	0.13400
$c_{NO}$	0.05090
$L_{char}$	5.0 m
$Re_{char}$	$1.574 \times 10^6$

**Table 4:** Initial conditions to the reentry capsule problem

Property	Value
$M_{initial}$	10.6
$\rho_{initial}$	0.02863 kg/m <sup>3</sup>
$p_{initial}$	3,885 Pa
$U_{initial}$	4,628 m/s
$T_{initial}$	473 K
Altitude	40,000 m
$c_N$	$10^{-9}$
$c_O$	0.07955
$c_{O_2}$	0.13400
$c_{NO}$	0.05090
$L_{char}$	3.0 m
$Re_{char}$	$3.468 \times 10^6$

**Table 5:** Values of theoretical stagnation pressure

Problem:	$M_{initial}$ :	$pr_0/pr_\infty$ :	$pr_\infty$ :	$pr_0$ (Theoretical):
Blunt body	8.78	99.98	1.709	170.87
Double ellipse	15.00	290.20	7.109	2,063.03
Reentry capsule	10.60	145.46	9.664	1,405.73

**Table 6:** Values of stagnation pressure and respective errors (Inviscid case/5<sup>th</sup> Order)

Physical Problem:	Scheme:	Spectral Method:	$pr_0$ : (Numerical)	Error:
	VL <sup>(1)</sup>	Chebyshev-Gauss-Radau	174.18	1.94
	LS <sup>(2)</sup>	Chebyshev-Gauss-Radau	166.38	2.63
	VL	Chebyshev-Gauss-Lobatto	149.43	12.55





Blunt Body ( $pr_0 = 170.87$ )	LS	Chebyshev-Gauss-Lobatto	153.67	10.07
	VL	Legendre-Gauss-Radau	115.05	32.67
	LS	Legendre-Gauss-Radau	133.17	22.06
	VL	Legendre-Gauss-Lobatto	103.12	39.65
	LS	Legendre-Gauss-Lobatto	126.41	26.02
	VL	Chebyshev-Gauss-Radau	1,932.44	6.33
	LS	Chebyshev-Gauss-Radau	-	-
	VL	Chebyshev-Gauss-Lobatto	1,729.63	16.16
Double Ellipse ( $pr_0 = 2,063.03$ )	LS	Chebyshev-Gauss-Lobatto	-	-
	VL	Legendre-Gauss-Radau	1,503.87	27.10
	LS	Legendre-Gauss-Radau	-	-
	VL	Legendre-Gauss-Lobatto	1,372.28	33.48
	LS	Legendre-Gauss-Lobatto	-	-
	VL	Chebyshev-Gauss-Radau	1,449.15	3.09
	LS	Chebyshev-Gauss-Radau	1,448.48	3.04
Reentry Capsule ( $pr_0 = 1,405.73$ )	VL	Chebyshev-Gauss-Lobatto	1,314.24	6.51
	LS	Chebyshev-Gauss-Lobatto	1,341.76	4.55
	VL	Legendre-Gauss-Radau	1,088.94	22.54
	LS	Legendre-Gauss-Radau	1,189.14	15.41
	VL	Legendre-Gauss-Lobatto	1,020.51	27.40
	LS	Legendre-Gauss-Lobatto	1,142.78	18.71

(1): Van Leer; (2): Liou and Steffen Jr.

**Table 7:** Values of stagnation pressure and respective errors (Viscous case/8<sup>th</sup> Order)

Physical Problem:	Scheme:	Spectral Method:	$pr_0$ : (Numerical)	Error:
Blunt Body ( $pr_0 = 170.87$ )	VL	Chebyshev-Gauss-Radau	190.60	11.55
	LS	Chebyshev-Gauss-Radau	179.95	5.31
	VL	Chebyshev-Gauss-Lobatto	178.03	4.19
	LS	Chebyshev-Gauss-Lobatto	173.22	1.38
	VL	Legendre-Gauss-Radau	138.87	18.73
	LS	Legendre-Gauss-Radau	148.38	13.16
	VL	Legendre-Gauss-Lobatto	139.81	18.18
	LS	Legendre-Gauss-Lobatto	148.98	12.81
	VL	Chebyshev-Gauss-Radau	2,125.22	3.01
	LS	Chebyshev-Gauss-Radau	-	-
Double Ellipse ( $pr_0 = 2,063.03$ )	VL	Chebyshev-Gauss-Lobatto	1,986.64	3.70
	LS	Chebyshev-Gauss-Lobatto	-	-
	VL	Legendre-Gauss-Radau	1,566.15	24.08
	LS	Legendre-Gauss-Radau	-	-
	VL	Legendre-Gauss-Lobatto	1,577.82	23.53
	LS	Legendre-Gauss-Lobatto	-	-
	VL	Chebyshev-Gauss-Radau	1,544.33	9.86
Reentry Capsule ( $pr_0 = 1,405.73$ )	LS	Chebyshev-Gauss-Radau	-	-
	VL	Chebyshev-Gauss-Lobatto	1,465.82	4.27
	LS	Chebyshev-Gauss-Lobatto	1,428.14	1.59
	VL	Legendre-Gauss-Radau	1,145.09	18.54
	LS	Legendre-Gauss-Radau	1,241.77	11.66
	VL	Legendre-Gauss-Lobatto	1,152.23	18.03
	LS	Legendre-Gauss-Lobatto	1,246.38	11.34



**Table 8:** Values of the lift aerodynamic coefficient (Inviscid case/5<sup>th</sup> Order)

Physical Problem:	Scheme:	Spectral Method:	$c_L$ :
Blunt Body	VL	Chebyshev-Gauss-Radau	$2.4119 \times 10^{-14}$
	LS	Chebyshev-Gauss-Radau	$4.9828 \times 10^{-14}$
	VL	Chebyshev-Gauss-Lobatto	$3.1569 \times 10^{-15}$
	LS	Chebyshev-Gauss-Lobatto	$4.9611 \times 10^{-14}$
	VL	Legendre-Gauss-Radau	$-8.6265 \times 10^{-15}$
	LS	Legendre-Gauss-Radau	$-1.9946 \times 10^{-15}$
	VL	Legendre-Gauss-Lobatto	$2.0275 \times 10^{-14}$
	LS	Legendre-Gauss-Lobatto	$8.0730 \times 10^{-15}$
Reentry Capsule	VL	Chebyshev-Gauss-Radau	$-1.9161 \times 10^{-9}$
	LS	Chebyshev-Gauss-Radau	$-5.7801 \times 10^{-10}$
	VL	Chebyshev-Gauss-Lobatto	$-1.1127 \times 10^{-9}$
	LS	Chebyshev-Gauss-Lobatto	$-5.1492 \times 10^{-10}$
	VL	Legendre-Gauss-Radau	$1.7507 \times 10^{-11}$
	LS	Legendre-Gauss-Radau	$-2.9437 \times 10^{-10}$
	VL	Legendre-Gauss-Lobatto	$8.4973 \times 10^{-11}$
	LS	Legendre-Gauss-Lobatto	$-2.8148 \times 10^{-10}$

**Table 9:** Values of the lift aerodynamic coefficient (Viscous case/8<sup>th</sup> Order)

Physical Problem:	Scheme:	Spectral Method:	$c_L$ :
Blunt Body	VL	Chebyshev-Gauss-Radau	$-3.8028 \times 10^{-15}$
	LS	Chebyshev-Gauss-Radau	$-1.4280 \times 10^{-14}$
	VL	Chebyshev-Gauss-Lobatto	$-7.3918 \times 10^{-15}$
	LS	Chebyshev-Gauss-Lobatto	$1.6481 \times 10^{-14}$
	VL	Legendre-Gauss-Radau	$-8.8229 \times 10^{-16}$
	LS	Legendre-Gauss-Radau	$5.2758 \times 10^{-15}$
	VL	Legendre-Gauss-Lobatto	$-2.8952 \times 10^{-15}$
	LS	Legendre-Gauss-Lobatto	$-1.7776 \times 10^{-14}$
Reentry Capsule	VL	Chebyshev-Gauss-Radau	$-8.1837 \times 10^{-11}$
	LS	Chebyshev-Gauss-Radau	-
	VL	Chebyshev-Gauss-Lobatto	$-6.0673 \times 10^{-11}$
	LS	Chebyshev-Gauss-Lobatto	$1.1448 \times 10^{-3}$
	VL	Legendre-Gauss-Radau	$-1.4515 \times 10^{-10}$
	LS	Legendre-Gauss-Radau	$-1.8391 \times 10^{-4}$
	VL	Legendre-Gauss-Lobatto	$-1.4144 \times 10^{-10}$
	LS	Legendre-Gauss-Lobatto	$-1.8245 \times 10^{-4}$

**Table 10:** Computational data (Inviscid case/5<sup>th</sup> Order)

Physical Problem:	Scheme:	Spectral Method:	CFL:	Iterations:
Blunt Body	VL	Chebyshev-Gauss-Radau	0.50	526
	LS	Chebyshev-Gauss-Radau	0.70	344
	VL	Chebyshev-Gauss-Lobatto	0.70	223
	LS	Chebyshev-Gauss-Lobatto	0.70	289
	VL	Legendre-Gauss-Radau	0.50	241
	LS	Legendre-Gauss-Radau	0.50	292
	VL	Legendre-Gauss-Lobatto	0.50	225
	LS	Legendre-Gauss-Lobatto	0.50	263
	VL	Chebyshev-Gauss-Radau	0.08	3,174



Double Ellipse	LS	Chebyshev-Gauss-Radau	-	-
	VL	Chebyshev-Gauss-Lobatto	0.20	981
	LS	Chebyshev-Gauss-Lobatto	-	-
	VL	Legendre-Gauss-Radau	0.20	535
	LS	Legendre-Gauss-Radau	-	-
	VL	Legendre-Gauss-Lobatto	0.20	545
Reentry Capsule	LS	Legendre-Gauss-Lobatto	-	-
	VL	Chebyshev-Gauss-Radau	0.30	968
	LS	Chebyshev-Gauss-Radau	0.30	1,392
	VL	Chebyshev-Gauss-Lobatto	0.30	918
	LS	Chebyshev-Gauss-Lobatto	0.30	1,130
	VL	Legendre-Gauss-Radau	0.30	610
	LS	Legendre-Gauss-Radau	0.30	757
	VL	Legendre-Gauss-Lobatto	0.30	459
	LS	Legendre-Gauss-Lobatto	0.30	656

**Table 11:** Computational data (Viscous case/8<sup>th</sup> Order)

Physical Problem:	Scheme:	Spectral Method:	CFL:	Iterations:
Blunt Body	VL	Chebyshev-Gauss-Radau	0.70	448
	LS	Chebyshev-Gauss-Radau	0.70	378
	VL	Chebyshev-Gauss-Lobatto	0.50	511
	LS	Chebyshev-Gauss-Lobatto	0.70	327
	VL	Legendre-Gauss-Radau	0.30	399
	LS	Legendre-Gauss-Radau	0.50	245
	VL	Legendre-Gauss-Lobatto	0.30	410
	LS	Legendre-Gauss-Lobatto	0.50	250
	VL	Chebyshev-Gauss-Radau	0.06	9,888
	LS	Chebyshev-Gauss-Radau	-	-
Double Ellipse	VL	Chebyshev-Gauss-Lobatto	0.10	4,824
	LS	Chebyshev-Gauss-Lobatto	-	-
	VL	Legendre-Gauss-Radau	0.10	2,762
	LS	Legendre-Gauss-Radau	-	-
	VL	Legendre-Gauss-Lobatto	0.10	2,939
	LS	Legendre-Gauss-Lobatto	-	-
Reentry Capsule	VL	Chebyshev-Gauss-Radau	0.10	3,806
	LS	Chebyshev-Gauss-Radau	-	-
	VL	Chebyshev-Gauss-Lobatto	0.10	3,965
	LS	Chebyshev-Gauss-Lobatto	0.10	4,242
	VL	Legendre-Gauss-Radau	0.10	1,696
	LS	Legendre-Gauss-Radau	0.10	2,722
	VL	Legendre-Gauss-Lobatto	0.10	1,848
LS	Legendre-Gauss-Lobatto	0.10	2,751	

**Table 12:** Computational cost of spectral variants

Order of Accuracy:	Scheme:	Spectral Method:	Computational Cost (seconds/volumes/iterations):
5 <sup>th</sup> Order	VL	Chebyshev-Gauss-Radau	0.0001373
	LS	Chebyshev-Gauss-Radau	0.0001358
	VL	Chebyshev-Gauss-Lobatto	0.0001408
	LS	Chebyshev-Gauss-Lobatto	0.0001385



(Inviscid case)	VL	Legendre-Gauss-Radau	0.0001352
	LS	Legendre-Gauss-Radau	0.0001344
	VL	Legendre-Gauss-Lobatto	0.0001361
	LS	Legendre-Gauss-Lobatto	0.0001373
	VL	Chebyshev-Gauss-Radau	0.0003688
	LS	Chebyshev-Gauss-Radau	0.0003717
	VL	Chebyshev-Gauss-Lobatto	0.0002980
	LS	Chebyshev-Gauss-Lobatto	0.0003793
8 <sup>th</sup> Order			
(Viscous case)	VL	Legendre-Gauss-Radau	0.0003689
	LS	Legendre-Gauss-Radau	0.0003684
	VL	Legendre-Gauss-Lobatto	0.0002967
	LS	Legendre-Gauss-Lobatto	0.0003721

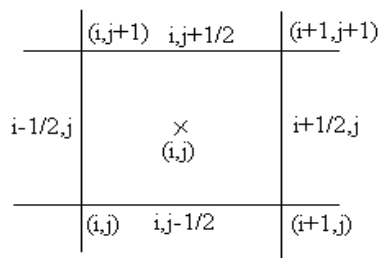


Figure 1: Computational cell

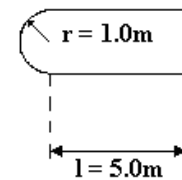


Figure 2: Blunt body configuration

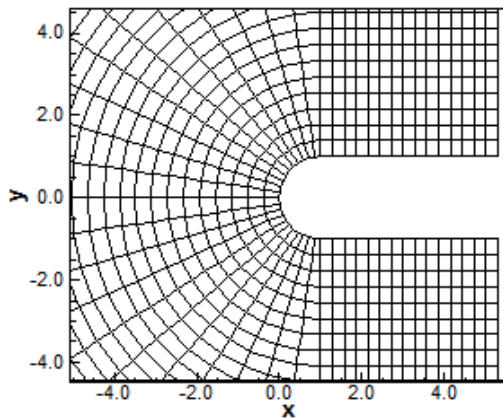


Figure 3: Blunt body inviscid mesh

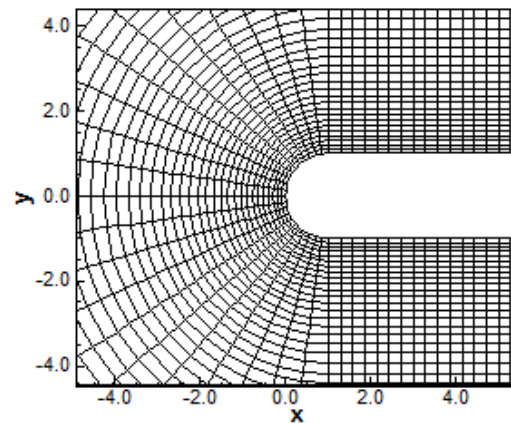


Figure 4: Blunt body viscous mesh

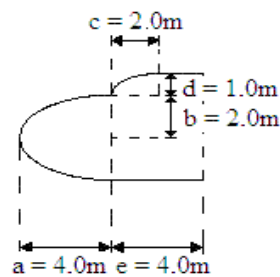


Figure 5: Double ellipse configuration

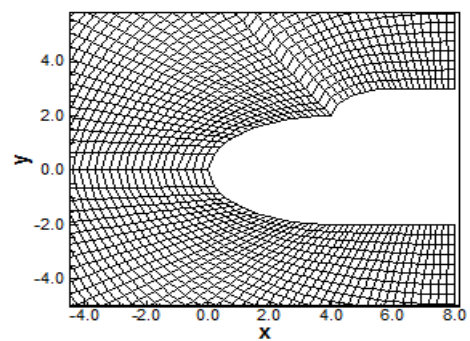


Figure 6: Double ellipse inviscid mesh



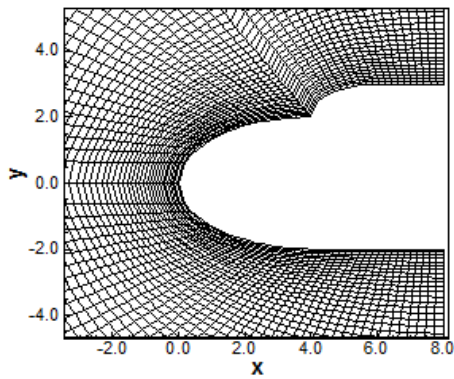


Figure 7: Double ellipse viscous mesh

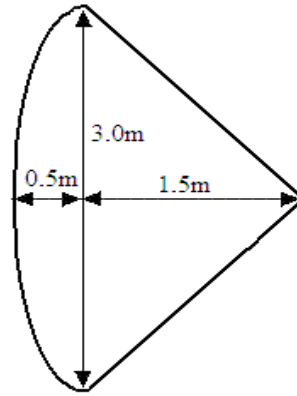


Figure 8: Reentry capsule configuration

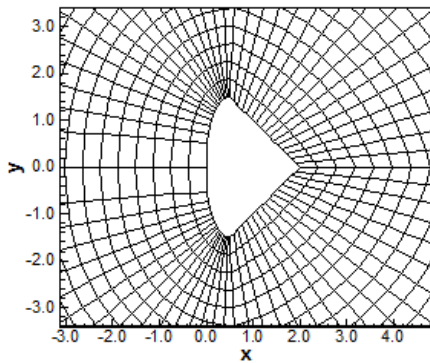


Figure 9: Reentry capsule inviscid mesh

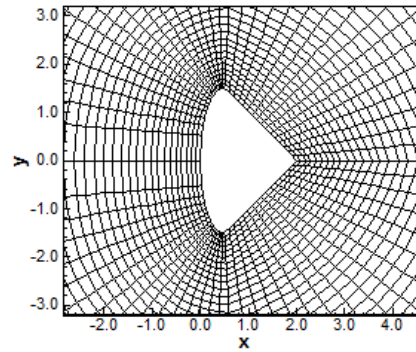


Figure 10: Reentry capsule viscous mesh

**Blunt Body Inviscid Solutions**

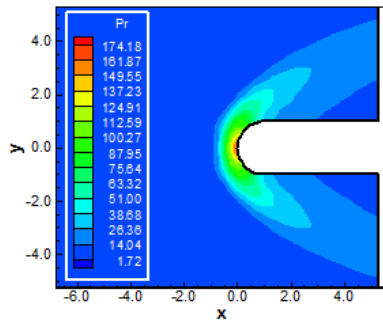


Figure 11: Pressure contours (CGR-VL)

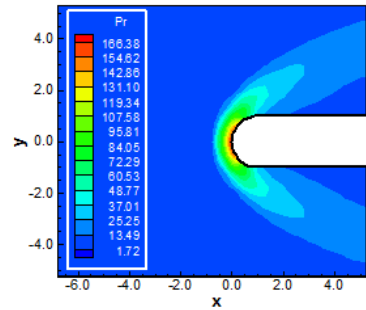


Figure 12: Pressure contours (CGR-LS)

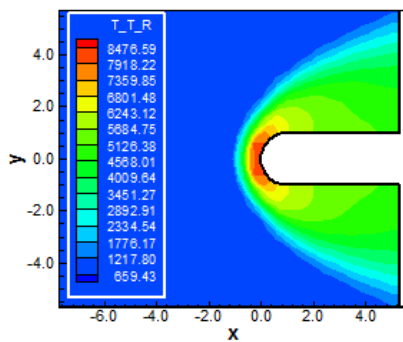


Figure 13: Translational/rotational temperature contours (CGR-VL)

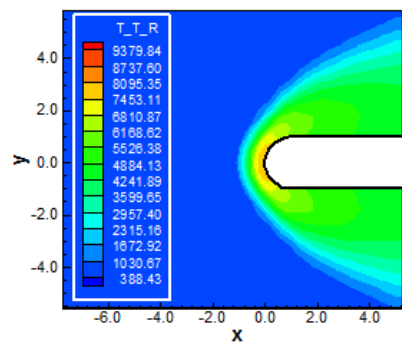


Figure 14: Translational/rotational temperature contours (CGR-LS)

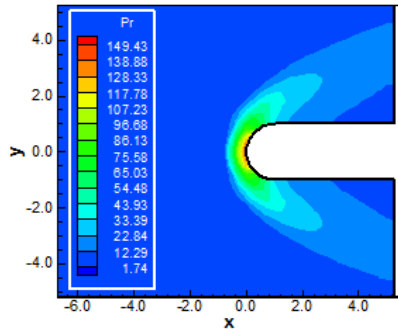


Figure 15: Pressure contours (CGL-VL)

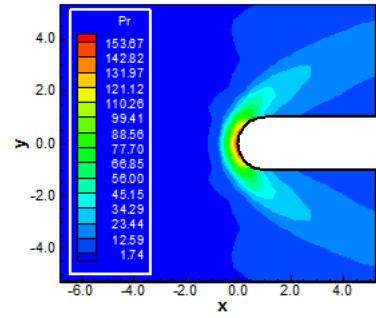


Figure 16: Pressure contours (CGL-LS)

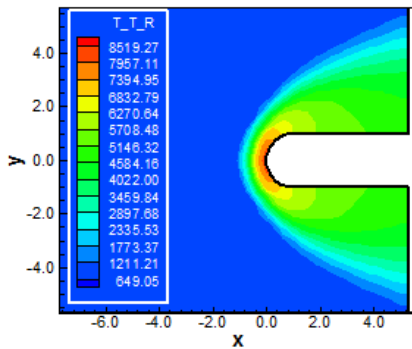


Figure 17: Translational/rotational temperature contours (CGL-VL)

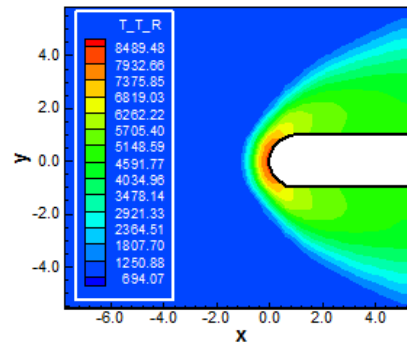


Figure 18: Translational/rotational temperature contours (CGL-LS)

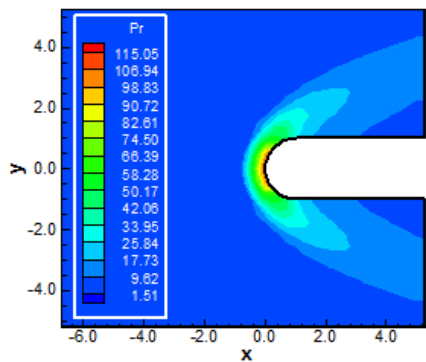


Figure 19: Pressure contours (LGR-VL)

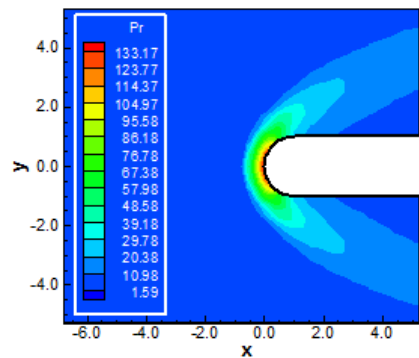


Figure 20: Pressure contours (LGR-LS)

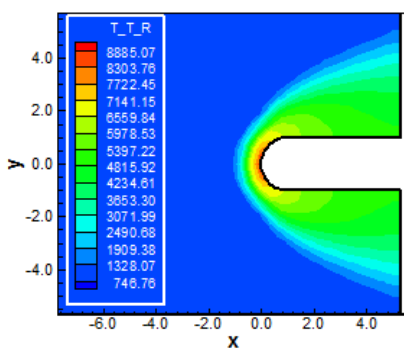


Figure 21: Translational/rotational temperature contours (LGR-VL)

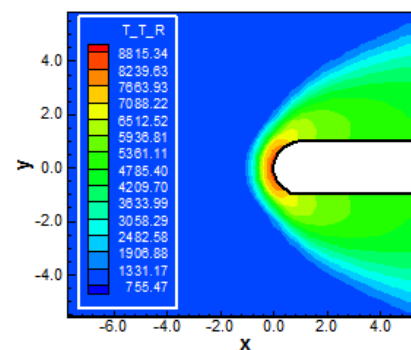


Figure 22: Translational/rotational temperature contours (LGR-LS)



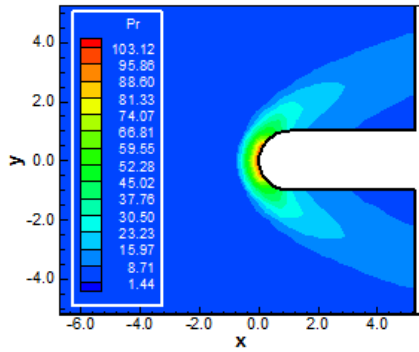


Figure 23: Pressure contours (LGL-VL)

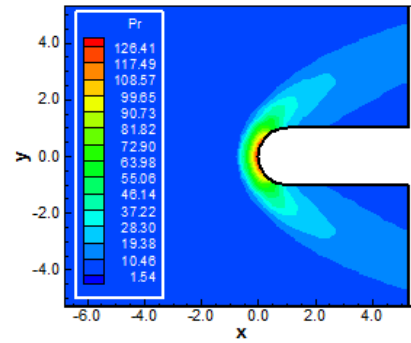


Figure 24: Pressure contours (LGL-LS)

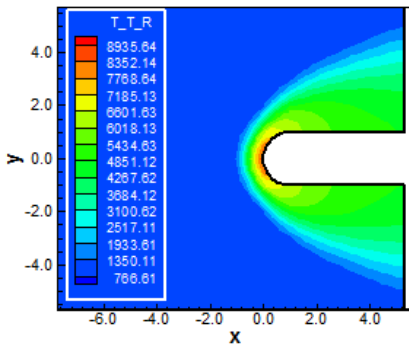


Figure 25: Translational/rotational temperature contours (LGL-VL)

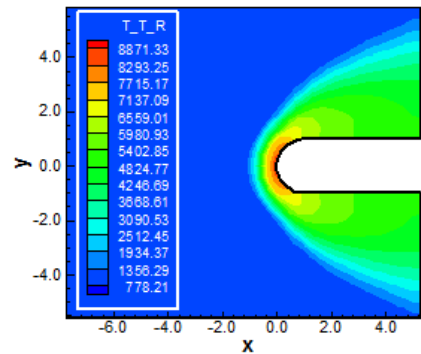


Figure 26: Translational/rotational temperature contours (LGL-LS)

**Blunt Body Viscous Solutions**

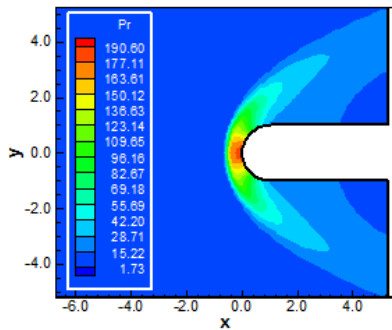


Figure 27: Pressure contours (CGR-VL)

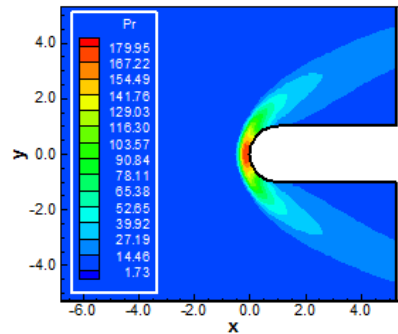


Figure 28: Pressure contours (CGR-LS)

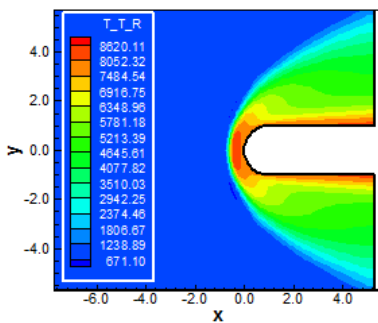


Figure 29: Translational/rotational temperature contours (CGR-VL)

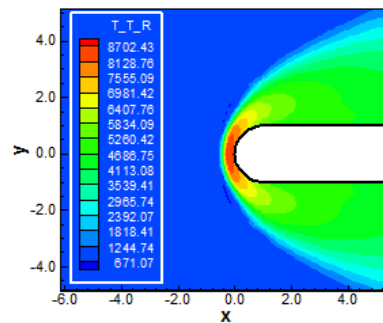


Figure 30: Translational/rotational temperature contours (CGR-LS)



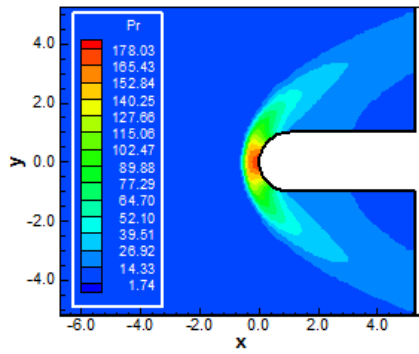


Figure 31: Pressure contours (CGL-VL)

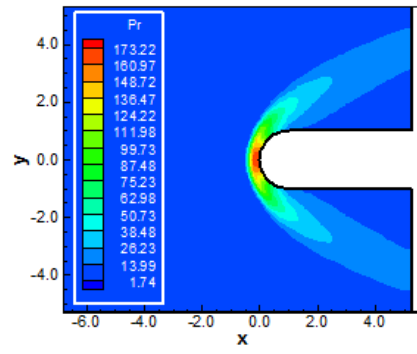


Figure 32: Pressure contours (CGL-LS)

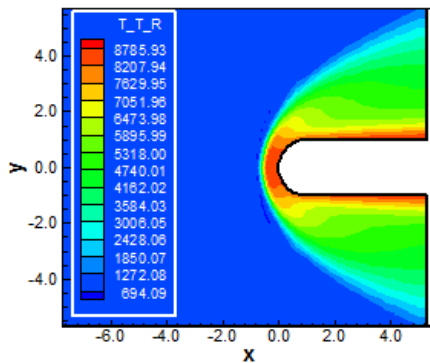


Figure 33: Translational/rotational temperature contours (CGL-VL)

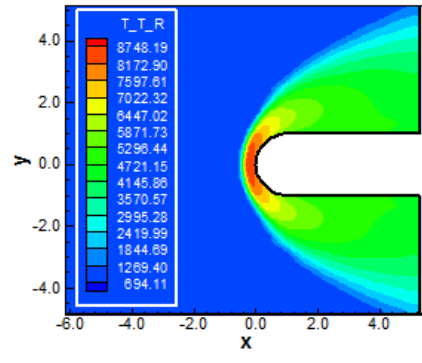


Figure 34: Translational/rotational temperature contours (CGL-LS)

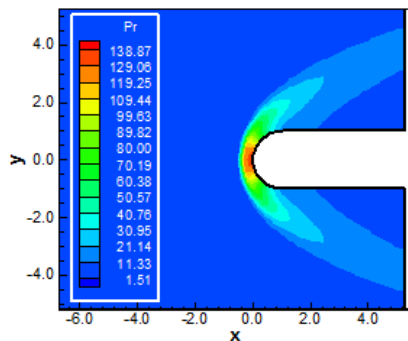


Figure 35: Pressure contours (LGR-VL)

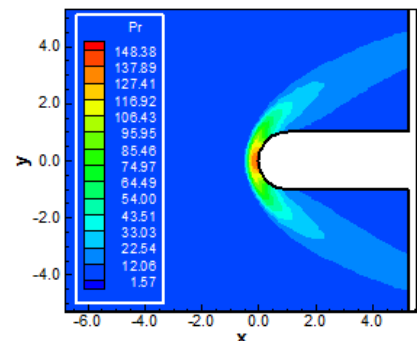


Figure 36: Pressure contours (LGR-LS)

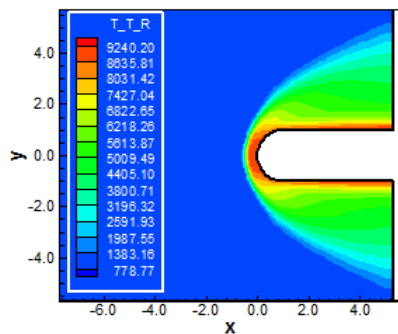


Figure 37: Translational/rotational temperature contours (LGR-VL)

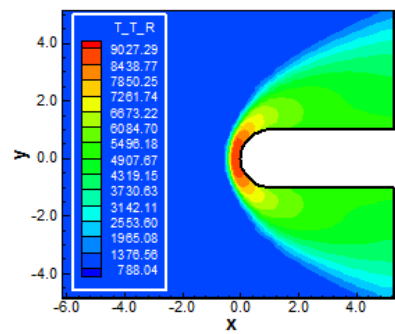


Figure 38: Translational/rotational temperature contours (LGR-LS)





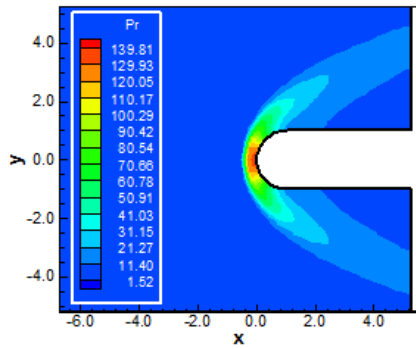


Figure 39: Pressure contours (LGL-VL)

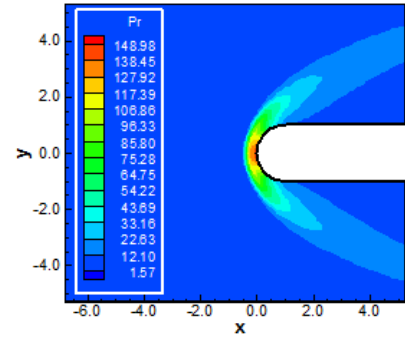


Figure 40: Pressure contours (LGL-LS)

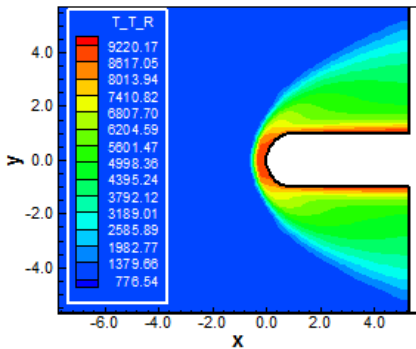


Figure 41: Translational/rotational temperature contours (LGL-VL)

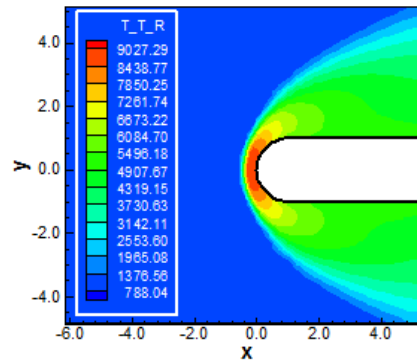


Figure 42: Translational/rotational temperature contours (LGL-LS)

**Double Ellipse Inviscid Solutions**

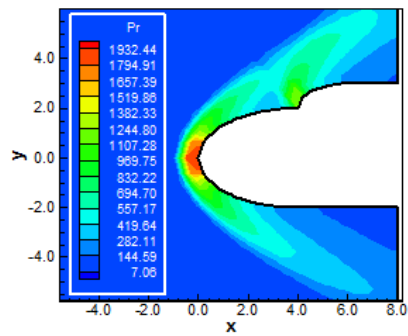


Figure 43: Pressure contours (CGR-VL)

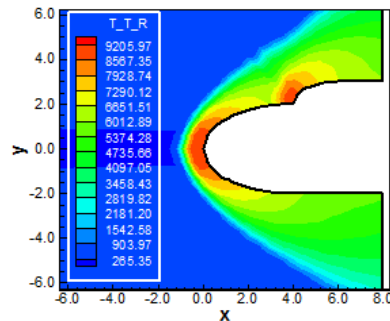


Figure 44: Translational/rotational temperature contours (CGR-VL)

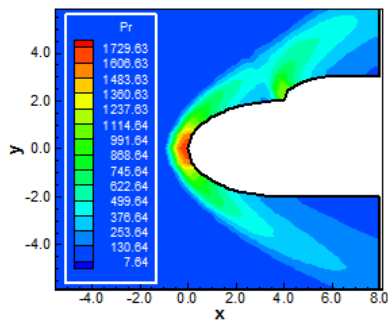


Figure 45: Pressure contours (CGL-VL)

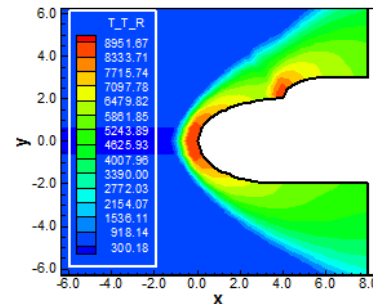


Figure 46: Translational/rotational temperature contours (CGL-VL)



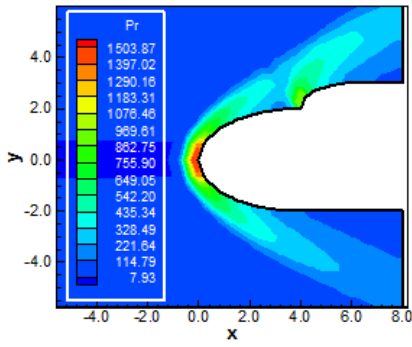


Figure 47: Pressure contours (LGR-VL)

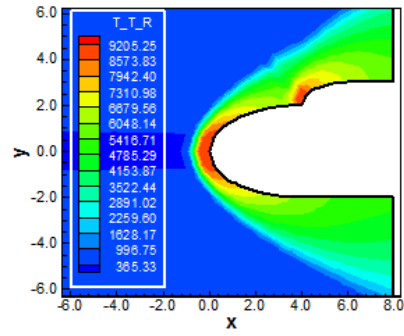


Figure 48: Translational/rotational temperature contours (LGR-VL)

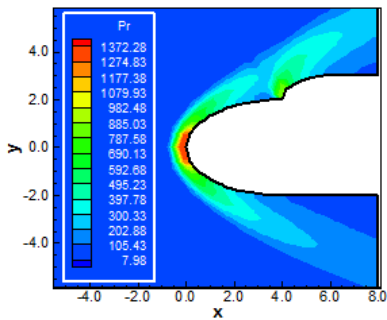


Figure 49: Pressure contours (LGL-VL)

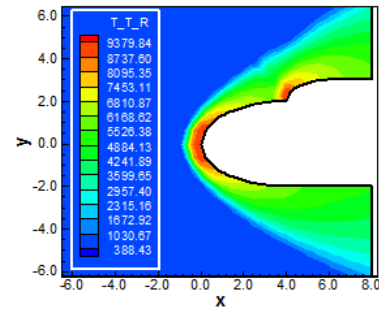


Figure 50: Translational/rotational temperature contours (LGL-VL)

**Double Ellipse Viscous Solutions**

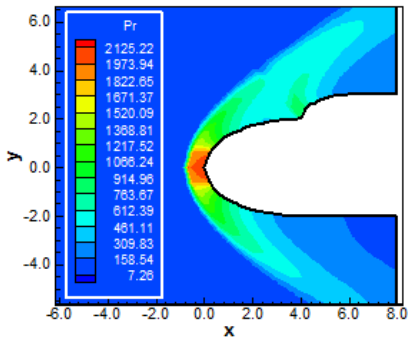


Figure 51: Pressure contours (CGR-VL)

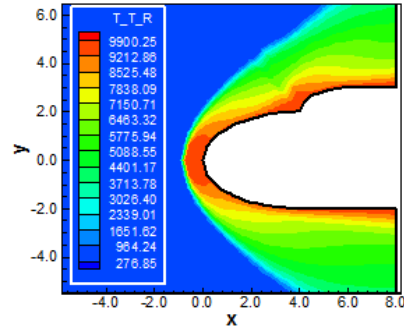


Figure 52: Translational/rotational temperature contours (CGR-VL)

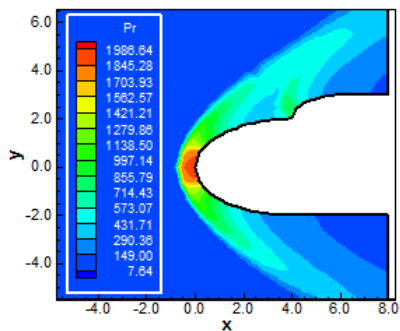


Figure 53: Pressure contours (CGL-VL)

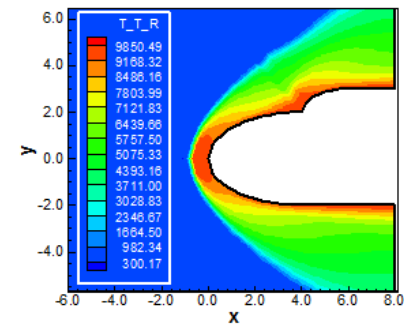


Figure 54: Translational/rotational temperature contours (CGL-VL)



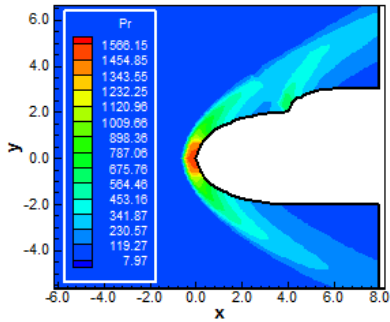


Figure 55: Pressure contours (LGR-VL)

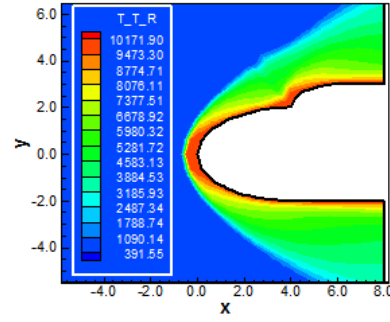


Figure 56: Translational/rotational temperature contours (LGR-VL)

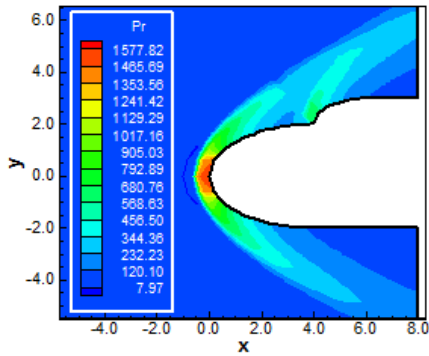


Figure 57: Pressure contours (LGL-VL)

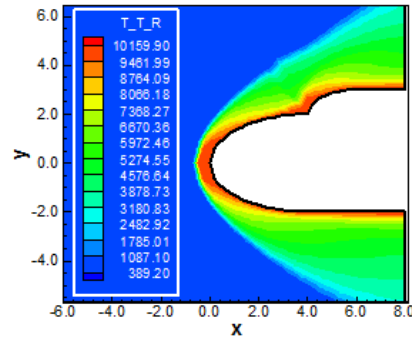


Figure 58: Translational/rotational temperature contours (LGL-VL)

**Reentry Capsule Inviscid Solutions**

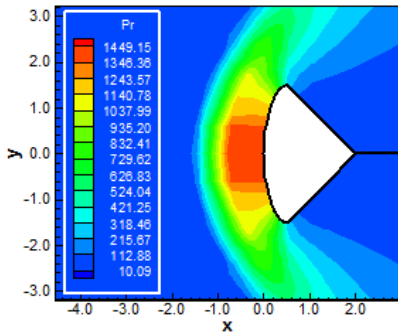


Figure 59: Pressure contours (CGR-VL)

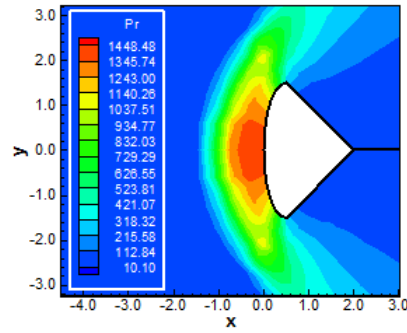


Figure 60: Pressure contours (CGR-LS)

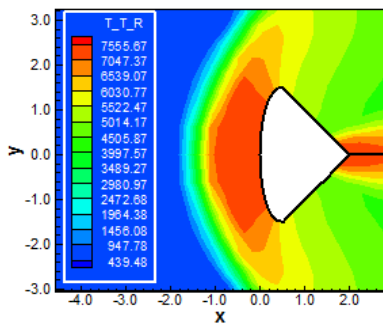


Figure 61: Translational/rotational temperature contours (CGR-VL)

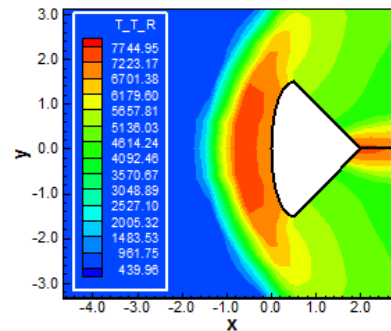


Figure 62: Translational/rotational temperature contours (CGR-LS)



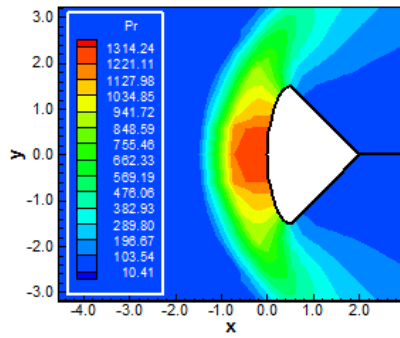


Figure 63: Pressure contours (CGL-VL)

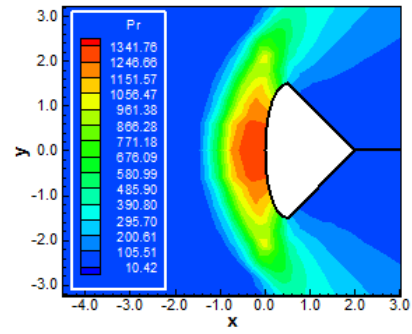


Figure 64: Pressure contours (CGL-LS)

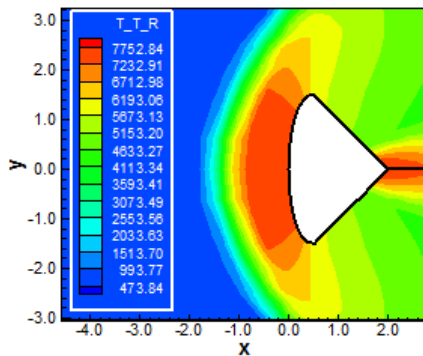


Figure 65: Translational/rotational temperature contours (CGL-VL)

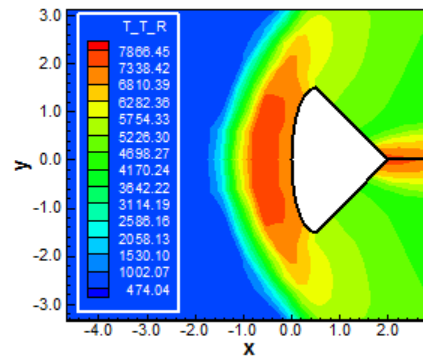


Figure 66: Translational/rotational temperature contours (CGL-LS)

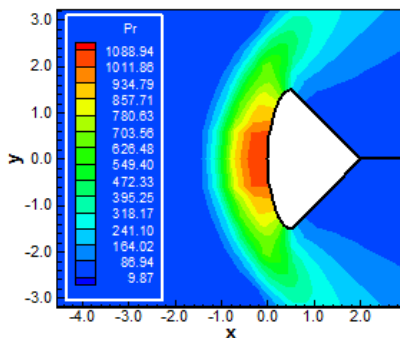


Figure 67: Pressure contours (LGR-VL)

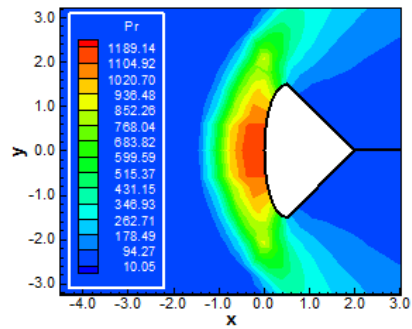


Figure 68: Pressure contours (LGR-LS)

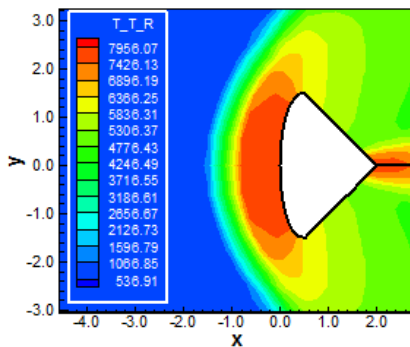


Figure 69: Translational/rotational temperature contours (LGR-VL)

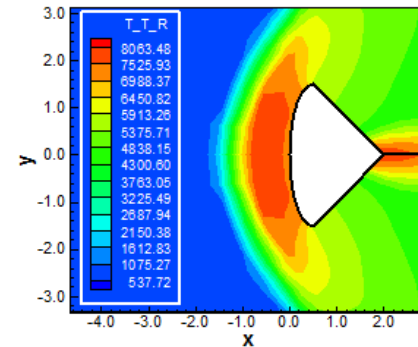


Figure 70: Translational/rotational temperature contours (LGR-LS)

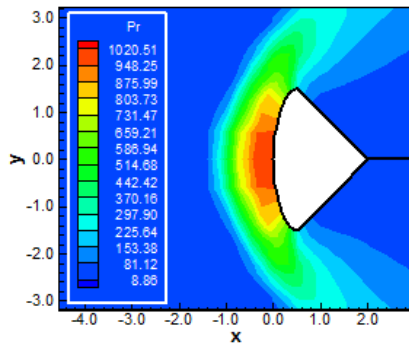


Figure 71: Pressure contours (LGL-VL)

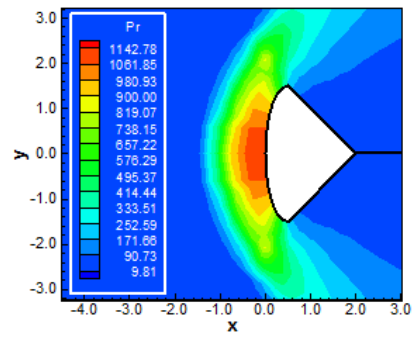


Figure 72: Pressure contours (LGL-LS)

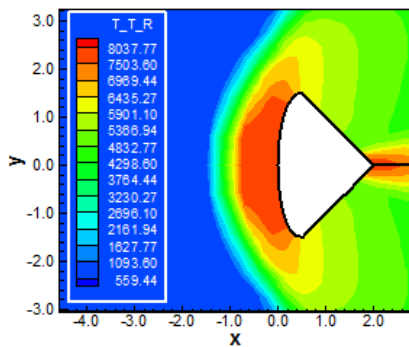


Figure 73: Translational/rotational temperature contours (LGL-VL)

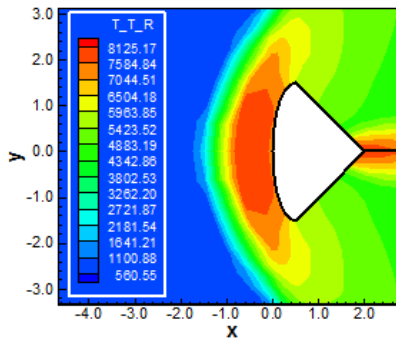


Figure 74: Translational/rotational temperature contours (LGL-LS)

**Reentry Capsule Viscous Solutions**

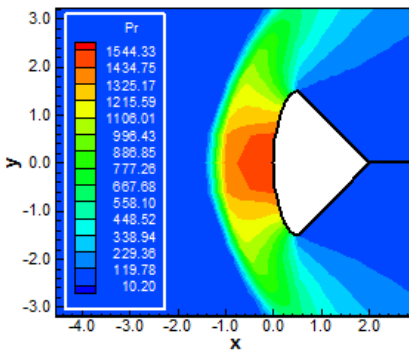


Figure 75: Pressure contours (CGR-VL)

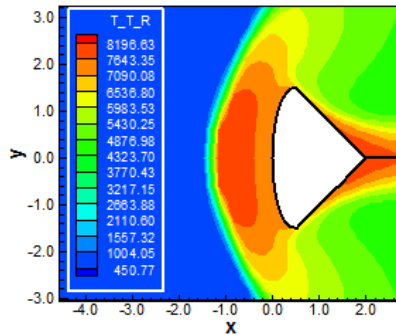


Figure 76: Translational/rotational temperature contours (CGR-VL)

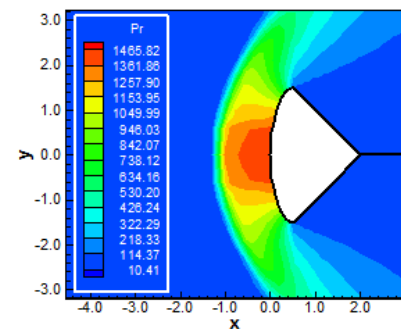


Figure 77: Pressure contours (CGL-VL)

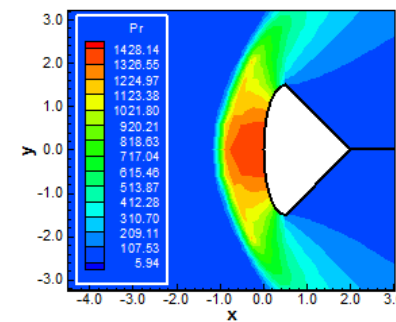


Figure 78: Pressure contours (CGL-LS)



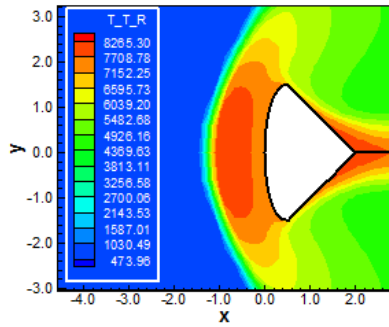


Figure 79: Translational/rotational temperature contours (CGL-VL)

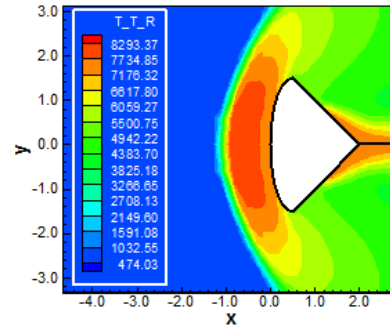


Figure 80: Translational/rotational temperature contours (CGL-LS)

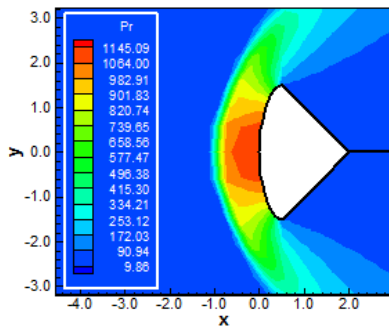


Figure 81: Pressure contours (LGR-VL)

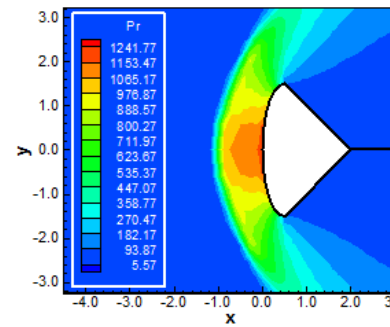


Figure 82: Pressure contours (LGR-LS)

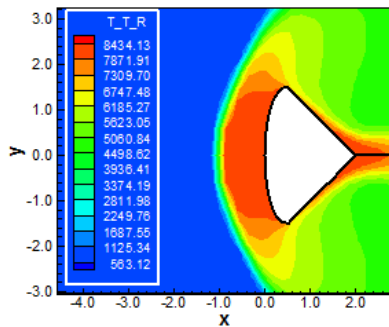


Figure 83: Translational/rotational temperature contours (LGR-VL)

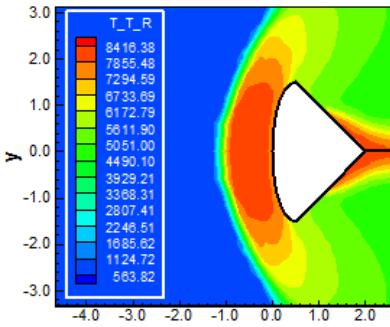


Figure 84: Translational/rotational temperature contours (LGR-LS)

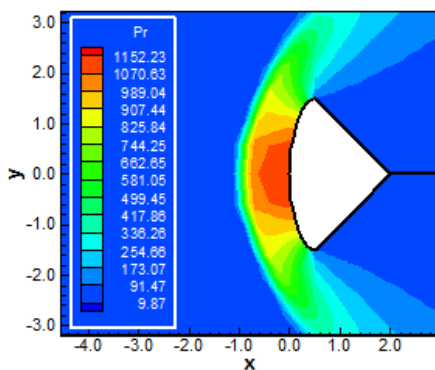


Figure 85: Pressure contours (LGL-VL)

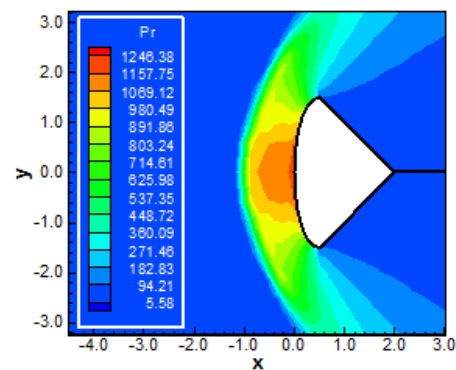


Figure 86: Pressure contours (LGL-LS)

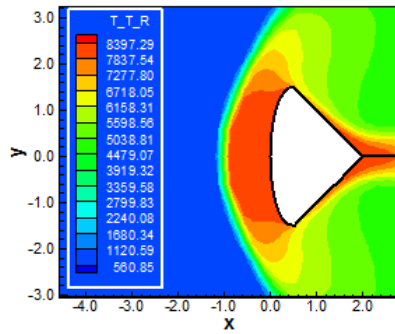


Figure 87: Translational/rotational temperature contours (LGL-VL)

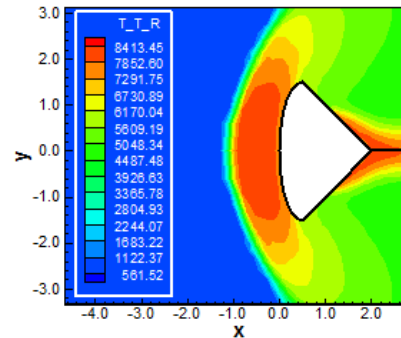


Figure 88: Translational/rotational temperature contours (LGL-LS)

### Computational Performance

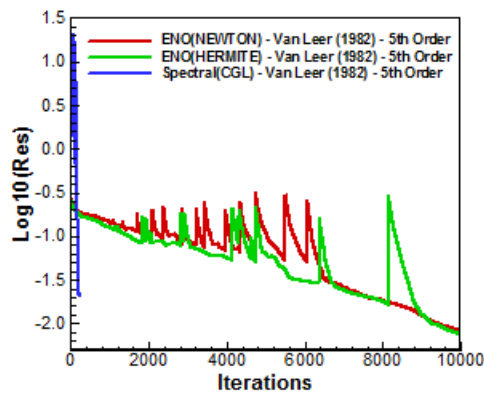


Figure 89: Convergence history comparisons (VL)

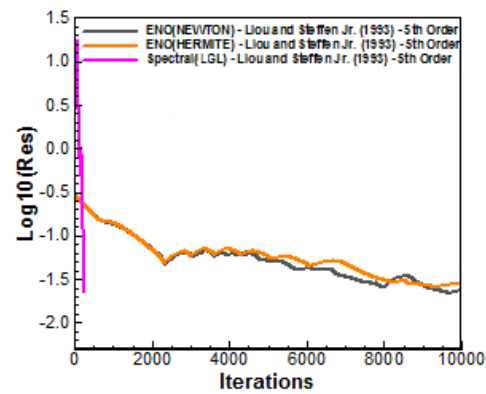


Figure 90: Convergence history comparisons (LS)

## 9. Conclusions

In the present work, a study involving spectral method to solve the reactive Euler and Navier-Stokes equations was performed. The Euler and Navier-Stokes equations, in conservative and finite volume contexts, employing structured spatial discretization, on a condition of thermochemical non-equilibrium, were studied. The spectral method presented in this work employed collocation points and variants of Chebyshev and Legendre interpolation functions were analyzed. High-order studies were accomplished to verify the accuracy of the spectral method. The “hot gas” hypersonic flows around a blunt body, around a double ellipse, and around a reentry capsule in two-dimensions were simulated. The [28-29] flux vector splitting algorithms were applied to execute the numerical experiments. The Euler backward integration method was employed to march the schemes in time. The convergence process was accelerated to steady state condition through a spatially variable time step procedure, which had proved effective gains in terms of computational acceleration (see [30-31]). The reactive simulations involved Earth atmosphere chemical model of five species and seventeen reactions, based on the [32] model. N, O, N<sub>2</sub>, O<sub>2</sub>, and NO species were used to accomplish the numerical comparisons. The results have indicated that the Chebyshev collocation point variants are more accurate in terms of stagnation pressure estimations. Errors inferior to 16.16% were found for this parameter in the inviscid case, while inferior to 11.55% for the viscous case. The Legendre collocation point variants are more accurate in terms of the lift coefficient estimations. Moreover, the Legendre collocation point variants are more computationally efficient and cheaper.

As final conclusion, it is possible to highlight that, for the blunt body problem, the [29] scheme in the viscous case using Chebyshev-Gauss-Lobatto collocation points had the best performance in estimating the stagnation pressure, and the lift aerodynamic coefficient was best estimated by the [28] scheme as using the Legendre-Gauss-Radau collocation points; for the double ellipse problem, the [28] scheme in the viscous case using



Chebyshev-Gauss-Radau collocation points had the best performance in estimating the stagnation pressure; and finally, for the reentry capsule problem, the [29] scheme in the viscous case using Chebyshev-Gauss-Lobatto collocation points had the best performance in estimating the stagnation pressure, and the lift aerodynamic coefficient was best estimated by the [28] scheme as using the Legendre-Gauss-Radau collocation points. Moreover, the best performance of the numerical schemes, for the 5<sup>th</sup> order of accuracy, was due to the [28] one, when using the Chebyshev-Gauss-Lobatto collocation points, employing a CFL of 0.70, and converging in 223 iterations, in the blunt body problem, whereas for the 8<sup>th</sup> order of accuracy, the best performance of the numerical schemes was due to the [29] one, when using the Legendre-Gauss-Radau collocation points, employing a CFL of 0.50, and converging in 245 iterations, also in the blunt body problem.

Finally, to close this work, the computational cost of the numerical schemes using the several types of collocation points is presented in Tab. 12. For the inviscid case, the cheapest combination was the [29] scheme using Legendre-Gauss-Radau collocation points with a cost of 0.0001344 sec/per-volume/per-iteration, whereas for the viscous case the cheapest was due to the [28] scheme coupled with the Legendre-Gauss-Lobatto collocation points with a cost of 0.0002967 sec/per-volume/per-iteration.

### **10. Motivation and Novelty**

The motivation to study spectral methods applied to reentry flow was enormous because of some papers in the CFD literature report for such methods as the state of art of high order resolution. The intention of this paper was to propose a different spectral method that was of easy implementation and conformed about author's ideas of treating the governing equations of fluid flow. The formulation presented here is for a thermochemical non-equilibrium condition and a two-temperature model. The comparisons involving the residual histories of ENO and of spectral method were very important to confirm that our numerical implementation was correct and also the potentiality of the method. Three physical problems were also a challenge that we accepted to lead with. The results with good accuracy represent a motivation to extend the present formulation to more species and different chemical conditions.

The novelty of the present study was to implement this different spectral method to treat thermochemical non-equilibrium reentry flows and to formulate the appropriate equations for accepting this method. The robustness and convergence features of this spectral method are very impressive. While the author had to use CFL numbers of order 0.01 for his ENO explicit methods, CFL numbers as great as 0.70 for his explicit spectral method were of common use. The proposed spectral method is different from the standard spectral ones on a sense that in the latter, the differential equations and the solution method are discretized with spectral tools, whereas in the former, only the vector of conserved variables and the convective fluxes should be discretized according to the spectral tools. The result is a robust and fast solver to treat the fluid-dynamic of reentry flows.

### **11. Future Works**

For the future, the author should extend the present formulation for a seven species chemical model under the condition of thermochemical non-equilibrium in two-dimensions. After that, they should extend to eleven species in two-dimensions until to arrive to the desired three-dimensional studies. Moreover, its implementation with turbulence effects and magnetic field actuation, that the author consider as the state of the art project, is an objective to be reached, in both, two- and three-dimensions. Finally, the interpretation of the present formulation to two-dimensional unstructured studies is also a goal to be reached.

### **Acknowledgments**

The author would like to thank the ITA facilities that allowed the realization of this work. He would also like to thank the CAPES by the financial support conceded under the form of a scholarship.

### **References**

- [1]. Barnes CJ, Huang GP, Shang JS. A high resolution spectral method for the compressible Navier-Stokes equations. AIAA Paper 2011-0049; 2011.





- [2]. Huang P, Wang ZJ, Liu Y. An implicit space-time spectral difference method for discontinuity capturing using adaptive polynomials. AIAA Paper 2005-5255; 2005.
- [3]. Huang P. High order discontinuity capturing using adaptive polynomials. AIAA Paper 2006-0305; 2006.
- [4]. Steger JL, Warming RF. Flux vector splitting of the inviscid gas dynamic equations with application to finite difference methods. *Journal of Computational Physics*.1981; 40: 263-293.
- [5]. Hughes T. The finite element method, linear static and dynamic finite element analysis, Prentice-Hall, Inc.
- [6]. Lele S. Compact finite difference schemes with spectral-like resolution. *Journal of Computational Physics*.1991; 103: 16-42.
- [7]. Gottlieb D, Orszag S. Numerical analysis of spectral methods: theory and applications. Society for industrial and applied mathematics, Philadelphia.
- [8]. Hussaini MY, Kopriva DA, Salas MD, Zang TA. Spectral methods for the Euler equations: Part I – Fourier methods and shock capturing. *AIAA Journal*. 1985; 23(1): 64-70.
- [9]. Slater JC. Electronic energy bands in metal. *Physical Review*.1934; 45: 794-801.
- [10]. Barta J. Über die näherungsweise Lösung einiger zweidimensionaler Elastizitätsaufgaben. *Zeitschrift für Angewandte Mathematik und Mechanik*.1937; 17: 184-185.
- [11]. Frazer RA, Jones WP, Skan SW. Approximation to functions and to the solutions of differential equations. Aeronautical Research Council, London. R&M 1799; 1937.
- [12]. Lanczos CL. Trigonometric interpolation of empirical and analytic functions. *Journal of Mathematics and Physics*.1938; 17: 123-199.
- [13]. Gottlieb D, Lustman L, Orszag SA. Spectral calculations of one-dimensional inviscid compressible flows. *SIAM Journal of Scientific and Statistical Computation*.1981; 2: 296-310.
- [14]. Taylor TD, Meyers RB, Albert JH. Pseudospectral calculations of shock waves, rarefaction waves and contact surfaces. *Computers and Fluids*.1981; 9: 469-473.
- [15]. Zang TA, Hussaini MY. Mixed spectral-finite difference approximations for slightly viscous flows. *Proceedings of the 7<sup>th</sup> International Conference on Numerical Methods in Fluid Dynamics*. Edited by W. C. Reynolds and R. W. MacCormack. *Lecture Notes in Physics*.1981; (141): 461-466.
- [16]. Narayan JR, Girimaji SS. Turbulent reacting flow computations including turbulence-chemistry interactions. AIAA Paper 92-0342; 1992.
- [17]. Gnoffo PA, Gupta RN, Shinn JL. Conservation equations and physical models for hypersonic flows in thermal and chemical nonequilibrium. NASA TP 2867; 1989.
- [18]. Liu M, Vinokur M. Upwind algorithms for general thermo-chemical nonequilibrium flows. AIAA Paper 89-0201; 1989.
- [19]. Park C. Radiation enhancement by nonequilibrium in Earth's atmosphere. *Journal of Spacecraft and Rockets*.1985; 22(1): 27-36.
- [20]. Park C. Problem of rate chemistry in the flight regimes of aeroassisted orbital transfer vehicles. *Thermal design of aeroassisted orbital transfer vehicles*. Progress in Astronautics and Aeronautics. Edited by H. F. Nelson, AIAA, NY.1985; 96: 511-537.
- [21]. Gnoffo PA. Three-dimensional AOTV flow fields in chemical nonequilibrium. AIAA Paper 86-0230; 1986.
- [22]. Li CP. Implicit methods for computing chemically reacting flow. NASA TM-58274; 1986.
- [23]. Lee JH. Basic governing equations for the flight regimes of aeroassisted orbital transfer vehicles. *Thermal design of aeroassisted transfer vehicles*. Progress in Astronautics and Aeronautics, AIAA.1985; 96: 3-53.
- [24]. Park C. Convergence of computation of chemically reacting flows. *Thermophysical aspects of reentry flows*. Progress in Astronautics and Aeronautics. Edited by J. N. Moss and C. D. Scott, AIAA, NY.1986; 103: 478-513.
- [25]. Park C. Assessment of two-temperature kinetic model for dissociating and weakly-ionizing nitrogen. AIAA Paper 86-1347; 1986.



- [26]. Park C. Calculation of nonequilibrium radiation in the flight regimes of aeroassisted orbital transfer vehicles. Thermal design of aeroassisted orbital transfer vehicles. Progress in Astronautics and Aeronautics. Edited by H. F. Nelson, AIAA, NY.1985; 96: 395-418.
- [27]. Park C. Nonequilibrium air radiation (NEQAIR) program: User's manual. NASA TM-86707; 1985.
- [28]. Van Leer B. Flux-vector splitting for the Euler equations. Lecture Notes in Physics, Springer Verlag, Berlin.1982; 170: 507-512.
- [29]. Liou M, and Steffen Jr. CJ.A new flux splitting scheme. Journal of Computational Physics, 1993; 107: 23-39.
- [30]. Maciel ESG. Simulations in 2D and 3D applying unstructured algorithms, Euler and Navier-Stokes equations – Perfect gas formulation. Saarbrücken, Deutschland: Lambert Academic Publishing (LAP). 2015; Ch. 1: 26-47.
- [31]. Maciel ESG. Simulations in 2D and 3D applying unstructured algorithms, Euler and Navier-Stokes equations – Perfect gas formulation. Saarbrücken, Deutschland: Lambert Academic Publishing (LAP). 2015; Ch. 6: 160-181.
- [32]. Saxena SK, Nair MT. An improved Roe scheme for real gas flow. AIAA Paper 2005-0587; 2005.
- [33]. Hussaini MY, Streett CL, Zang TA. Spectral methods for partial differential equations. ICASE Report No. 83-46; 1983.
- [34]. Davis PA, Rabinowitz P. Numerical integration. Blaisdell Publishing Co.; 1967.
- [35]. Canuto C, Hussaini MY, Quarteroni A, Zang TA. Spectral methods evolution to complex geometries and applications to fluid dynamics. Scientific Computation Springer; 2007.
- [36]. Prabhu RK. An implementation of a chemical and thermal nonequilibrium flow solver on unstructured meshes and application to blunt bodies. NASA CR-194967; 1994.
- [37]. Maciel ESG. Hypersonic reactive flow simulations in two-dimensions, chemical and thermochemical non-equilibrium conditions. Saarbrücken. Deutschland: Lambert Academic Publishing (LAP). 2015; Ch. 3:174-247.
- [38]. Maciel ESG. Hypersonic reactive flow simulations in two-dimensions, chemical and thermochemical non-equilibrium conditions. Saarbrücken. Deutschland: Lambert Academic Publishing (LAP). 2015; Ch. 4: 248-332.
- [39]. Ait-Ali-Yahia D, Habashi WG. Finite element adaptive method for hypersonic thermochemical nonequilibrium flows. AIAA Journal.1997; 35(8): 1294-1302.
- [40]. Radespiel R, Kroll N. Accurate flux vector splitting for shocks and shear layers. Journal of Computational Physics.1995; 121: 66-78.
- [41]. Long LN, Khan MMS, Sharp HT. Massively parallel three-dimensional Euler / Navier-Stokes method. AIAA Journal. 1991; 29(5): 657-666.
- [42]. Vincent WG, Kruger Jr.CH. Introduction to physical gas dynamics. Malabar, Florida, EUA: Krieger Publishing Company. 2002; Ch. 1: 1-26.
- [43]. Fox RW, McDonald AT. Introdução à mecânica dos fluidos. Guanabara Editor; 1988.
- [44]. Maciel ESG. Simulação numérica de escoamentos supersônicos e hipersônicos utilizando técnicas de dinâmica dos fluidos computacional. Doctoral Thesis. ITA, CTA, São José dos Campos, SP, Brazil; 2002.
- [45]. Maciel ESG. High order comparison between flux vector splitting schemes on the reentry flow context. Computational and Applied Mathematics Journal. 2015; 1(4): 225-248.
- [46]. Maciel ESG. Comparison between Newton and Hermite ENO interpolations as applied to reentry flows in 2D. Computational and Applied Mathematics Journal. 2015; 1(5): 261-281.
- [47]. Maciel ESG. Comparison among MUSCL, ENO and WENO procedures as applied to reentry flows in 2D. Computational and Applied Mathematics Journal. 2015; 1(5): 355-377.
- [48]. Anderson Jr. JD. Fundamentals of aerodynamics. McGraw-Hill, Inc., 5<sup>th</sup> Edition, 1008p.; 2010.

